

Introduction to stochastic geometry

Bruno Figliuzzi

February 11, 2026

Contents

1	Morphological models	1
1.1	Introduction	1
1.2	Basic facts from mathematical morphology	2
1.2.1	Dilation and erosion	2
1.2.2	Opening and closing	5
1.2.3	Granulometry	7
1.3	Probabilistic approach and Choquet capacity	8
1.3.1	Covariance	9
1.4	Measurements on random sets	14
1.4.1	Minkowski functionals and intrinsic volumes	15
1.4.2	Steiner formulae	17
1.4.3	Stereology and Crofton formulae	18
1.5	Point processes	19
1.5.1	General theory	19
1.5.2	Poisson point process	23
1.5.3	Marked point processes	29
1.6	Germ-grain processes	31
1.6.1	Definition and first properties	31
1.6.2	Practical implementation	36
1.6.3	Statistical analysis for the Boolean model	37
1.6.4	Notes	42
1.7	Random Tessellations	42
1.7.1	General introduction	43
1.7.2	Poisson tessellation models	46
1.7.3	Poisson-Voronoi tessellations	48

2 Morphological models in materials science	53
2.1 Microstructure modelling with morphological models	54
2.1.1 Context	54
2.1.2 Experimental data	55
2.1.3 Morphological model	56
2.1.4 Results and discussions	59
2.1.5 Conclusion	61
2.2 Parameters estimation in morphological models	62
2.2.1 Problem statement	63
2.2.2 Bayesian formulation	64
2.2.3 Sampling from the posterior distribution	65
2.2.4 Numerical experiments	66
2.2.5 Conclusion	74
2.3 Eikonal based tessellations	75
2.3.1 Eikonal equation	75
2.3.2 Fast marching algorithm	76
2.3.3 Applications	77
2.3.4 Conclusion	81

Chapter 1

Morphological models

1.1 Introduction

The study of heterogeneous materials, ranging from porous media and composite structures to polycrystalline aggregates, relies heavily on understanding their complex internal microstructures. These microstructures, often characterized by intricate spatial arrangements of phases, grains, or inclusions, play a pivotal role in determining the macroscopic physical properties of materials. However, the sheer complexity and variability of real-world microstructures pose significant challenges for their direct analysis and simulation. To address these challenges, morphological models provide a robust mathematical framework for describing, analyzing, and simulating the geometry of heterogeneous media. Rooted in stochastic geometry and mathematical morphology, these models offer a powerful toolkit for capturing the essential features of microstructures, such as connectivity, size distribution, and spatial correlations, while accounting for their inherent randomness. This chapter explores the foundational concepts of morphological models, with a focus on their application to materials science. We begin by introducing the core principles of mathematical morphology, including dilation, erosion, opening, and closing operations, which serve as the building blocks for analyzing geometric structures. We then extend these concepts to a probabilistic framework, where random sets and point processes enable the modeling of microstructures as stochastic realizations. Special attention is given to germ-grain models, such as the Boolean model, and random tessellations, including Voronoi and Johnson-Mehl tessellations, which are widely

used to simulate realistic material microstructures. Beyond theoretical developments, this chapter also addresses practical aspects of morphological modeling, such as parameter estimation and statistical analysis. We discuss methods for inferring model parameters from experimental data, including the use of covariance functions, granulometries, and stereological techniques. These tools are essential for bridging the gap between theoretical models and real-world applications, enabling the generation of synthetic microstructures that faithfully reproduce the geometric characteristics of observed materials.

1.2 Basic facts from mathematical morphology

Mathematical morphology is a theory for the analysis and processing of geometrical structures. It is most commonly applied to digital images, but it can be employed as well on graphs, surface meshes, solids, and many other spatial structures. Random sets theory makes an extensive use of the concepts of mathematical morphology. It is therefore natural to start this introduction with some concepts of mathematical morphology.

1.2.1 Dilation and erosion

The basic idea behind mathematical morphology is to analyze a set A of some topological space E by probing it with a compact set K referred to as structuring element. Hence, mathematical morphology makes extensive use of classical operators of set theory, including for instance union or intersection. We first introduce the two basics bricks of mathematical morphology, namely erosion and dilation.

Definition 1.2.1. *Let A be a closed set in E . The dilated of the set A by the structuring element K is the set*

$$D^K(A) = \{x \in E | K_x \cap A \neq \emptyset\}, \quad (1.1)$$

where K_x is the translated of the compact K at $x \in E$. Similarly, the eroded of the set A by the structuring element K is the set

$$E^K(A) = \{x \in E | K_x \subset A\}. \quad (1.2)$$

Dilation and erosion are dual operators with respect to the complement, in the sense that dilating the set A by the structuring element K is equivalent to erode A^c by K .

We assume now that E is the euclidean space \mathbb{R}^d of dimension d . The vectorial space structure of \mathbb{R}^d allows us to define new operations on $\mathcal{P}(\mathbb{R}^d)$, namely the Minkowski addition and substraction.

Definition 1.2.2. *Let A and B be subsets of \mathbb{R}^d . The Minkowski addition is defined by*

$$A \oplus B = \{a + b, a \in A, b \in B\}. \quad (1.3)$$

The Minkowski addition is an associative and commutative operation. Note that $(\mathcal{P}(\mathbb{R}^d), \oplus)$ is an abelian semi-group, whose neutral element is $\{0\}$.

We introduce some notations at this point. Let x be a point of \mathbb{R}^d . We denote by A_x the set A translated at point x :

$$A_x = A \oplus \{x\}. \quad (1.4)$$

Similarly, we denote by \check{B} the symmetric set of $B \in \mathcal{P}(E)$ defined by

$$\check{B} = \{-x, x \in B\}. \quad (1.5)$$

Definition 1.2.3. *Using these notations, we can define the Minkowski substraction by duality. Let A and B be subsets of E . The Minkowski substraction is defined by*

$$A \ominus B = (A^c \oplus B)^c = \cap_{x \in B} A_x. \quad (1.6)$$

We can also express the classical dilation and erosion operators of mathematical morphology as functions of the Minkowski addition and substraction respectively.

Definition 1.2.4. *Let A and B be subsets of \mathbb{R}^d . The erosion of A by B yields the set*

$$\{x \in E, B_x \in A\} = A \ominus \check{B}. \quad (1.7)$$

Similarly, we can check by duality that the dilation of A by B yields the set

$$\{x \in E, B_x \cap A \neq \emptyset\} = A \oplus \check{B}. \quad (1.8)$$

Proposition 1.2.1. Let $A, B \in \mathcal{P}(\mathbb{R}^d)$ be subsets of \mathbb{R}^d , and K, K_1, K_2 be compact sets of $\mathcal{K}(\mathbb{R}^d)$. Then, we have

$$(A \ominus \check{K}_1) \ominus \check{K}_2 = A \ominus (\check{K}_1 \oplus \check{K}_2), \quad (1.9)$$

$$(A \cap B) \ominus \check{K} = (A \ominus \check{K}) \cap (B \ominus \check{K}), \quad (1.10)$$

and

$$A \oplus (\check{K}_1 \cup \check{K}_2) = (A \oplus \check{K}_1) \cup (A \oplus \check{K}_2). \quad (1.11)$$

Proof. To prove (1.9), we first note that, by definition,

$$A \ominus \check{K}_1 = (A^c \oplus \check{K}_1)^c$$

using the definition of the Minkowski subtraction. Therefore, we have:

$$\begin{aligned} (A \ominus \check{K}_1) \ominus \check{K}_2 &= (A^c \oplus \check{K}_1)^c \ominus \check{K}_2 \\ &= ((A^c \oplus \check{K}_1) \oplus \check{K}_2)^c \quad (\text{def. of Minkowski subtraction}) \\ &= (A^c \oplus (\check{K}_1 \oplus \check{K}_2))^c \quad (\text{associativity of Minkowski addition}) \\ &= A \ominus (\check{K}_1 \oplus \check{K}_2) \quad (\text{def. of Minkowski subtraction}) \end{aligned}$$

The relations (1.10) and (1.11) follow immediately from the definition of Minkowski addition and subtraction. \square

Proposition 1.2.2 (Minkowski operations and convexity). Let $A \in \mathcal{P}(\mathbb{R}^d)$ be a subset of \mathbb{R}^d , and K be a compact set of $\mathcal{K}(\mathbb{R}^d)$. Then :

1. If A is convex, then $A \ominus \check{K}$ is convex.
2. If A is convex and K is convex, then $A \oplus \check{K}$ is convex.

In other words, Minkowski subtraction preserves convexity for any compact K and Minkowski addition preserves convexity if K is convex.

Proof. We address each part separately.

1. Convexity of $A \ominus \check{K}$: Let $x_1, x_2 \in A \ominus \check{K}$ and $\lambda \in [0, 1]$. We want to show that

$$x_\lambda := \lambda x_1 + (1 - \lambda)x_2 \in A \ominus \check{K}.$$

By definition of Minkowski subtraction, for all $k \in \check{K}$ we have

$$x_1 + k \in A, \quad x_2 + k \in A.$$

Since A is convex, it follows that

$$\lambda(x_1 + k) + (1 - \lambda)(x_2 + k) = (\lambda x_1 + (1 - \lambda)x_2) + k = x_\lambda + k \in A.$$

As this holds for all $k \in \check{K}$, we conclude that

$$x_\lambda \in A \ominus \check{K}.$$

Hence, $A \ominus \check{K}$ is convex.

2. Convexity of $A \oplus \check{K}$:

Recall the definition of Minkowski addition:

$$A \oplus \check{K} = \{a + k : a \in A, k \in \check{K}\}.$$

Let $a_1 + k_1, a_2 + k_2 \in A \oplus \check{K}$ and $\lambda \in [0, 1]$. Consider the convex combination:

$$\lambda(a_1 + k_1) + (1 - \lambda)(a_2 + k_2) = (\lambda a_1 + (1 - \lambda)a_2) + (\lambda k_1 + (1 - \lambda)k_2).$$

Since A is convex, we have $\lambda a_1 + (1 - \lambda)a_2 \in A$. Thus, the convex combination belongs to $A \oplus \check{K}$ if and only if

$$\lambda k_1 + (1 - \lambda)k_2 \in \check{K}.$$

In other words, $A \oplus \check{K}$ is convex if \check{K} itself is convex.

□

1.2.2 Opening and closing

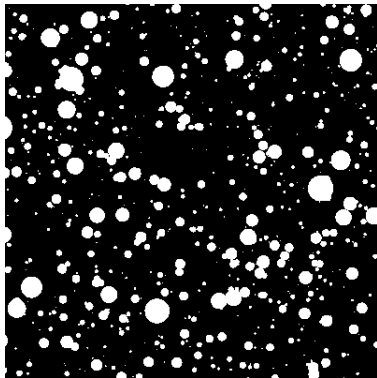
By combining erosion and dilation, we can define two new morphological operators. Let $A, B \in \mathcal{P}(E)$ be subsets of E . The *closing* A^B and the *opening* A_B of the set A by B are defined as follows:

$$A^B = (A \oplus \check{B}) \ominus B, \quad (1.12)$$

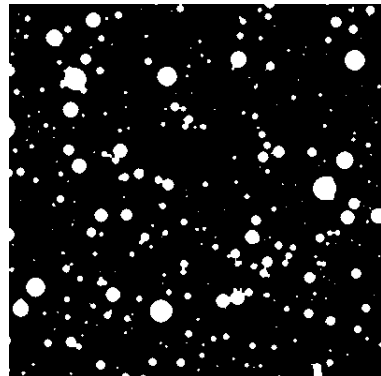
and

$$A_B = (A \ominus \check{B}) \oplus B. \quad (1.13)$$

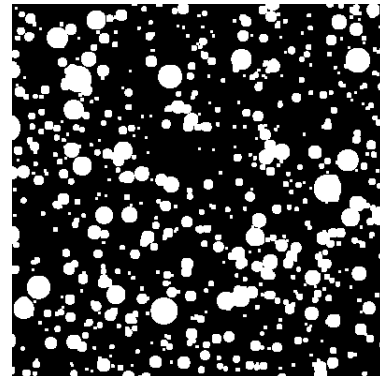
The opening and closing operators are widely used in mathematical morphology. These operator can for instance be used to perform image denoising and are the fundamental bricks upon which builds most of the theory.



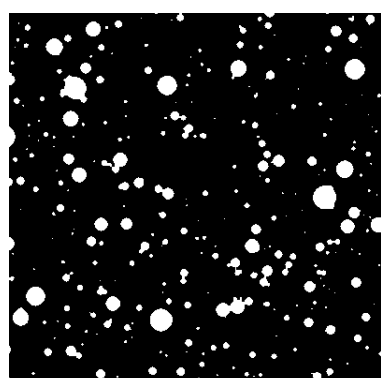
(a) Segmented microstructure simulated with VtkSim [13].



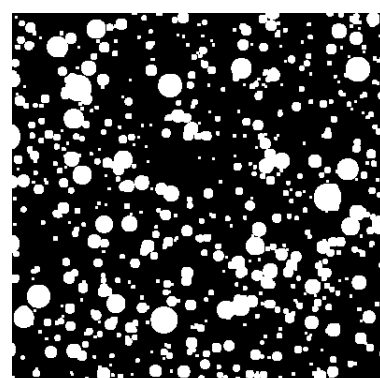
(b) Erosion



(c) Dilation



(d) Opening



(e) Closing

Figure 1.1: Morphological operations applied to a segmented microstructure using a disk of radius one pixel. Erosion removes the smallest components, while dilation expands them.

1.2.3 Granulometry

A first application of openings and closings related to the description of random sets are the granulometry operators. Intuitively, a granulometry by closing (resp. by opening) is a family of closings (resp. openings) of increasing sizes, which allows us to characterize the size distribution of the connected components of any random set.

Definition 1.2.5. *More formally, a granulometry is a family of set operators Φ_λ depending on a positive parameter λ satisfying the following properties:*

- For all A in $\mathcal{F}(E)$, $\Phi_\lambda(A) \subset A$: Φ_λ is anti-extensive.
- If $A \subset B$, then $\Phi_\lambda(A) \subset \Phi_\lambda(B)$: Φ_λ is increasing.
- $\Phi_\lambda \circ \Phi_\mu = \Phi_\mu \circ \Phi_\lambda = \Phi_{\max(\mu,\lambda)}$

The axiomatic of granulometries was first formulated by Matheron in [29]. Note that an immediate consequence of the last point of the definition is that Φ_λ is necessarily an idempotent operator, in the sense that $\Phi_\lambda \circ \Phi_\lambda = \Phi_\lambda$.

As stated above, the axiomatic of granulometries remains very general. In practice, we will often consider granulometries relying on a family of openings. Let K be a convex set. We consider the family $\{K_\lambda, \lambda > 0\}$, where $K_\lambda = \lambda K$. The operator

$$\Phi_\lambda(A) = (A \ominus \check{K}_\lambda) \oplus K_\lambda, \quad (1.14)$$

defined for all closed set A of $\mathcal{F}(E)$, is a granulometry. For a random set A , a granulometry by openings describes the size distribution of the elements of A by opening by convex sets.

In a similar manner, we can define a granulometry by closing. To that end, we consider the operator

$$\Phi_\lambda(A) = (A \oplus \check{K}_\lambda) \ominus K_\lambda, \quad (1.15)$$

defined for all closed set A of $\mathcal{F}(E)$. A granulometry by closing describes the size distribution of the elements of A by closing by convex sets.

1.3 Probabilistic approach and Choquet capacity

Concepts of mathematical morphology prove very convenient to study random sets. In particular, it is of interest to translate some compact set K in an observation window to analyse a random closed set A of \mathbb{R}^n . Two elementary events can occur:

- if $K \cap A = \emptyset$, the structuring element K is disjoint from A ;
- otherwise, if $K \cap A \neq \emptyset$, the structuring element K hits the set A .

The random closed set A is completely characterized by the functional $T(K)$ defined for all compact sets K by

$$T(K) = P\{A \cap K \neq \emptyset\} = 1 - P\{K \cap A^c\} = 1 - Q(K) \quad (1.16)$$

$T(K)$ is called the Choquet capacity of the random closed set A . Note that the Choquet capacity is closely related to dilation and erosion operators. For all compact set $K \subset \mathbb{R}^n$, we have indeed

$$T(K) = P\{K \cap A \neq \emptyset\} = P\{x \in A \oplus \check{K}\} \quad (1.17)$$

Proposition 1.3.1. *The Choquet capacity is related to the Minkowski operators by the following equation :*

$$Q(K) = P\{K \subset A^c\} = P\{x \in A^c \ominus \check{K}\}. \quad (1.18)$$

Proof. By definition, the functional $Q(K)$ is the probability that the compact set K is entirely contained in the complement of A :

$$Q(K) := P\{K \subset A^c\}.$$

Recall the definition of Minkowski subtraction (erosion) of a set B by a compact set K :

$$B \ominus \check{K} := \{x \in \mathbb{R}^n : x + \check{K} \subset B\}.$$

Let us apply this definition with $B = A^c$. Then, for any $x \in \mathbb{R}^n$,

$$x \in A^c \ominus \check{K} \iff x + \check{K} \subset A^c.$$

Now, notice that $\check{K} = \{-k : k \in K\}$. If we translate \check{K} by x , we get

$$x + \check{K} = \{x - k : k \in K\}.$$

Therefore, the event

$$\{x \in A^c \ominus \check{K}\}$$

is exactly the event that “the translated version of K by x lies entirely in A^c ”, which is equivalent (up to translation) to $K \subset A^c$. Hence, taking probabilities, we obtain

$$Q(K) = P\{K \subset A^c\} = P\{x \in A^c \ominus \check{K}\}.$$

This shows that the erosion of A^c by \check{K} describes exactly the event that K is contained in A^c , and thus

$$Q(K) = P\{x \in A^c \ominus \check{K}\}.$$

□

The structuring element K can be a single point $\{x\}$ of \mathbb{R}^n or any compact set of \mathbb{R}^n . However, we have to insist on the fact that the choice of structuring element is fundamental. Each compact set K indeed brings its own information on the studied set A . For instance, if one chooses K to be a single point, the choquet capacity yields

$$T(\{x\}) = P\{\{x\} \cap A \neq \emptyset\} = P\{x \in A\}, \quad (1.19)$$

which is the *spatial law* of the set A . Similarly, if one chooses K to be the set $\{x, x + h\}$, the choquet capacity allows to calculate the *covariance* of the random closed set.

$$T(\{x, x + h\}) = P\{x \in A, x + h \in A\}. \quad (1.20)$$

1.3.1 Covariance

The covariance is a - if not *the* - fundamental tool to describe spatial arrangement in a random closed set.

Definition 1.3.1. *The covariance of a random set $A \subset \mathbb{R}^n$ is the function C_A defined on $\mathbb{R}^n \times \mathbb{R}^n$ by*

$$C_A(x, x + h) = P\{x \in A, x + h \in A\}, \quad (1.21)$$

where h is some vector of \mathbb{R}^n .

The covariance of the set A at a given point x and for a distance h is the probability that x and $x + h$ both belong to A . Note that for a stationary random set, the covariance is a function of the distance h only:

$$C_A(x, x + h) = C_A(h). \quad (1.22)$$

If in addition the set A is ergodic, meaning that its spatial averages over a single realization are representative of ensemble averages over many realizations, the covariance $C(h)$ can be estimated from the volume fraction of $A \cap A_{-h}$ as

$$C_A(h) = P\{x \in A \cap A_{-h}\} = V(A \cap A_{-h}) = V(A \ominus \check{h}), \quad (1.23)$$

where h is the set $\{x, x + h\}$. In practice, this allows the covariance to be computed from a single experimental sample of the random set using equation (1.23), rather than requiring multiple realizations.

The covariance C_A provides useful information about the spatial arrangement of the random set A . In particular, it accounts for the presence of several scales in the studied set or for periodicity. Note that by definition, $C_A(0)$ simply corresponds to the volumic fraction of the set A . For any orientation, the covariance $C(h)$ reaches a sill at the distance or range h_∞ . At this distance, events $\{x \in A\}$ and $\{x + h_\infty\}$ are independent and we have

$$C_A(h_\infty) = p^2. \quad (1.24)$$

These considerations enable us to define a normalized version of the covariance that remains between 0 and 1:

$$\gamma(h) = \frac{C(h) - p^2}{p(1 - p)}. \quad (1.25)$$

For an ergodic experimental sample, the covariance can be estimated with relation (1.23). An alternative approach is to use the Fourier transform:

Proposition 1.3.2. *Let A be a subset of \mathbb{R}^d . Then, the covariance of A is*

$$C_A(h) = \frac{1}{(2\pi)^n} \int_{\mathbb{R}^n} |\hat{f}(\xi)|^2 \exp(i\xi h) d\xi. \quad (1.26)$$

Proof. Let $A \subset \mathbb{R}^n$ be a random closed set. Define its indicator function

$$f(x) := \mathbf{1}_A(x) = \begin{cases} 1, & x \in A, \\ 0, & x \notin A. \end{cases}$$

By definition, the covariance of A at a lag h is

$$C_A(h) = \mathbb{E}[f(x)f(x+h)].$$

Consider the Fourier transform of f , denoted by

$$\hat{f}(\xi) = \int_{\mathbb{R}^n} f(x)e^{-i\xi \cdot x} dx.$$

Recall the convolution theorem: for two functions f and g ,

$$\mathcal{F}[f * g] = \hat{f} \hat{g}, \quad \text{and} \quad f * g(x) = \int_{\mathbb{R}^n} f(y)g(x-y) dy.$$

The covariance can be expressed as a convolution:

$$C_A(h) = \int_{\mathbb{R}^n} f(x)f(x+h) dx = (f * f^\dagger)(h),$$

where $f^\dagger(x) := f(-x)$ is the reflection of f . Applying the Fourier transform, we have

$$\mathcal{F}[C_A](\xi) = \mathcal{F}[f * f^\dagger](\xi) = \hat{f}(\xi) \overline{\hat{f}(\xi)} = |\hat{f}(\xi)|^2,$$

where the overline denotes complex conjugation. Finally, applying the inverse Fourier transform gives

$$C_A(h) = \frac{1}{(2\pi)^n} \int_{\mathbb{R}^n} |\hat{f}(\xi)|^2 e^{i\xi \cdot h} d\xi.$$

□

The covariance of a random set A generally depends on the orientation of the vector h . The *isotropised covariance* is defined to be

$$\bar{C}(h) = \int_{S_{d-1}} C(h\mathbf{u})U(d\mathbf{u}), \tag{1.27}$$

where \mathbf{u} is an unitary vector and $U(d\mathbf{u})$ denotes the uniform distribution on the unit sphere S_{d-1} .

Some features of the covariance can easily be expressed analytically. A fundamental example is given by its first derivative.

Proposition 1.3.3. *Let A be a random set on \mathbb{R}^d . Then, the first derivative of the covariance is*

$$\frac{d}{dh}C_A(h\mathbf{u}) = -\lim_{h \rightarrow 0} \nu_{d-1}((K \cap K_{r\mathbf{u}})|_{\mathbf{u}^\perp}), \quad (1.28)$$

where ν_{d-1} is the Lebesgue measure on \mathbb{R}^{d-1} and \mathbf{u} is some unit vector. $(K \cap K_{r\mathbf{u}})|_{\mathbf{u}^\perp}$ denotes the projection of $(K \cap K_{r\mathbf{u}})$ on the hyperplane that has \mathbf{u} as normal vector.

Proof. Let $A \subset \mathbb{R}^d$ be a random closed set with covariance

$$C_A(h\mathbf{u}) = P\{x \in A, x + h\mathbf{u} \in A\},$$

where \mathbf{u} is a unit vector in \mathbb{R}^d . The proof proceeds in four subsequent steps:

1. *Covariance in terms of volume fractions:*

For a compact observation window $K \subset \mathbb{R}^d$, the covariance along the direction \mathbf{u} can be expressed as

$$C_A(h\mathbf{u}) = V(A \cap A_{h\mathbf{u}}),$$

where $A_{h\mathbf{u}}$ denotes the translation of A by $h\mathbf{u}$. This follows from ergodicity, as in equation (1.23).

2. *Difference quotient:*

The derivative of the covariance in the direction \mathbf{u} is formally

$$\frac{d}{dh}C_A(h\mathbf{u}) = \lim_{\Delta h \rightarrow 0} \frac{C_A((h + \Delta h)\mathbf{u}) - C_A(h\mathbf{u})}{\Delta h}.$$

Substituting the volume fraction expression, we get

$$\frac{d}{dh}C_A(h\mathbf{u}) = \lim_{\Delta h \rightarrow 0} \frac{V(A \cap A_{(h + \Delta h)\mathbf{u}}) - V(A \cap A_{h\mathbf{u}})}{\Delta h}.$$

3. *Geometric interpretation for $h \rightarrow 0$:*

For small Δh , the difference

$$V(A \cap A_{h\mathbf{u}}) - V(A \cap A_{(h + \Delta h)\mathbf{u}})$$

corresponds to the volume of the “boundary layer“ of thickness Δh where A and $A_{h\mathbf{u}}$ stop overlapping. By classical results in geometric measure theory (Steiner formula and Crofton formula, see section 1.4), this volume is approximately

$$\Delta h \cdot \nu_{d-1}((A \cap A_{h\mathbf{u}})|_{\mathbf{u}^\perp}) + o(\Delta h),$$

where ν_{d-1} is the $(d-1)$ -dimensional Lebesgue measure on the hyperplane orthogonal to \mathbf{u} , and $(A \cap A_{h\mathbf{u}})|_{\mathbf{u}^\perp}$ is the orthogonal projection of $A \cap A_{h\mathbf{u}}$ onto that hyperplane.

4. Taking the limit:

Dividing by Δh and taking the limit $\Delta h \rightarrow 0$, we obtain

$$\frac{d}{dh} C_A(h\mathbf{u}) = -\nu_{d-1}((A \cap A_{h\mathbf{u}})|_{\mathbf{u}^\perp}).$$

Finally, evaluating at $h \rightarrow 0$, the derivative of the covariance at zero lag is

$$\frac{d}{dh} C_A(h\mathbf{u}) \Big|_{h=0} = -\lim_{h \rightarrow 0} \nu_{d-1}((K \cap K_{h\mathbf{u}})|_{\mathbf{u}^\perp}),$$

where K is the compact observation window. Thus, the first derivative of the covariance along the direction \mathbf{u} is given by the negative $(d-1)$ -dimensional measure of the projection of the overlap region onto the hyperplane perpendicular to \mathbf{u} , which proves equation (1.28).

□

When $d = 3$, for the isotropic case, equation (1.28) simply yields

$$\frac{dC_A}{dh}(0) = -S(A), \quad (1.29)$$

where $S(A)$ is the surface area of the set A in \mathbb{R}^3 . Similarly, when $d = 2$, equation (1.28) yields

$$\frac{dC_A}{dh}(0) = -\mathcal{P}(A), \quad (1.30)$$

where $\mathcal{P}(A)$ is the length of the perimeter of A in \mathbb{R}^2 .

1.4 Measurements on random sets

Starting from a material image, it is possible to measure a very large number of parameters. It is, however, essential that these parameters be meaningful with respect to the physics and the geometry of the material. Two families of parameters are usually considered, namely *metric* and *topological* parameters. Intuitively, if we consider inclusions embedded in a matrix, one may be interested in the volume fraction of inclusions. This parameter is metric, in the sense that it is obtained directly through measurement. Conversely, one may also be interested in the number of included particles. This parameter is topological, as it is obtained by counting.

In practice, strict limitations are imposed on admissible measurements. First, one generally requires the measurement to be invariant under isometries. This ensures that a measurement performed on a set X does not depend on its location or orientation in space. A *homogeneity* condition must also be satisfied: if the same set X is observed at different scales, the measurement should scale accordingly. This condition yields, for a measurement W that is homogeneous of degree k ,

$$W(\lambda X) = \lambda^k W(X), \quad (1.31)$$

where $\lambda > 0$.

An additional requirement is *additivity*. In mathematical terms, this condition is expressed through the relation

$$W(X) + W(Y) = W(X \cup Y) + W(X \cap Y), \quad (1.32)$$

whenever the union $X \cup Y$ is admissible. Finally, the measurement should be *continuous*: small deformations of the measured set must not result in large variations of the measured value.

Finite unions of convex sets play a key role in stochastic geometry. Much of the geometric theory of random sets is built upon results obtained for convex sets and their extensions to finite unions of convex sets. A fundamental result states that all measurements satisfying the conditions listed above can be expressed as linear combinations of a finite number of basic functionals, known as Minkowski functionals. We discuss this result in greater depth in the following sections.

1.4.1 Minkowski functionals and intrinsic volumes

Definition 1.4.1. A subset C of \mathbb{R}^d is said to be convex if, for every pair of points $x, y \in C$ and every $c \in [0, 1]$, we have

$$cx + (1 - c)y \in C. \quad (1.33)$$

Affine linear subspaces provide archetypal examples of convex sets. An affine linear subspace L of dimension k in \mathbb{R}^d is a translation of a k -dimensional linear subspace and can be characterized as the solution set of $d - k$ independent affine equations. Such subspaces are commonly referred to as *k-flats* or *k-planes*.

Definition 1.4.2. A convex body is a compact, convex subset of \mathbb{R}^d . We denote by $\mathcal{C}(\mathbb{R}^d)$ the family of all convex bodies in \mathbb{R}^d .

Definition 1.4.3. A convex body functional is a functional h defined on $\mathcal{C}(\mathbb{R}^d)$ that assigns a real value $h(C)$ to each $C \in \mathcal{C}(\mathbb{R}^d)$. Such a functional is said to be:

- isometry-invariant if $h(\mathcal{G}C) = h(C)$ for every isometry \mathcal{G} ;
- monotone if $C_1 \subset C_2$ implies $h(C_1) \leq h(C_2)$;
- C -additive if, for all $C_1, C_2 \in \mathcal{C}(\mathbb{R}^d)$ such that $C_1 \cup C_2$ is convex, we have

$$h(C_1) + h(C_2) = h(C_1 \cup C_2) + h(C_1 \cap C_2). \quad (1.34)$$

A fundamental theorem of integral geometry states that all convex body functional that are isometry-invariant, monotone and C -additive can be expressed as linear combinations of the Minkowski functionals W_d . The Minkowski functionals are isometry-invariant, monotone, C -additive convex body functionals, defined directly on $\mathcal{C}(\mathbb{R}^d)$ by the formula

$$W_k(C) = \frac{b_d}{b_{d-k}} \int_{\mathbb{L}_k} \mu_{d-k}(C|_{E^\perp}) U_k(dE). \quad (1.35)$$

In this expression, b_k denotes the volume of the unit ball in \mathbb{R}^k . μ_k is the k -dimensional Lebesgue measure. \mathbb{L}_k is the set of all k -subspaces, $C|_{E^\perp}$ is the orthogonal projection of the convex body C on E^\perp , E^\perp is the $(d - k)$ -subspace orthogonal to $E \in \mathbb{L}_k$, and U_k is the uniform probability distribution on \mathbb{L}_k .

$\forall d > 0$, for $k = 0$, equation (1.35) becomes

$$W_0(C) = \int_{\mathbb{L}_0} \mu_d(C|_{E^\perp}) U_0(dE) = \mu_d(C). \quad (1.36)$$

Hence, $W_0(C)$ is equal to the volume $\mu_d(C)$.

Similarly, $\forall d > 0$, for $k = d$, we find

$$W_d(C) = b_d \quad (1.37)$$

Theorem 1.4.1 (Hadwiger's characterization theorem). *Every non-negative, isometry-invariant, monotone, and C -additive convex body functional h on $\mathcal{C}(\mathbb{R}^d)$ can be written uniquely as a linear combination of the Minkowski functionals:*

$$h(C) = \sum_{k=0}^d a_k W_k(C), \quad \forall C \in \mathcal{C}(\mathbb{R}^d), \quad (1.38)$$

where the coefficients a_k are real constants.

In dimensions $d = 1, 2, 3$, the Minkowski functionals admit the following explicit interpretations:

$\mathbf{d = 1}$	$W_0(C) = \mathcal{L}(C), \quad W_1(C) = 2$
$\mathbf{d = 2}$	$W_0(C) = \mathcal{A}(C), \quad W_1(C) = \frac{L(C)}{2},$ $W_2(C) = \pi$
$\mathbf{d = 3}$	$W_0(C) = \mathcal{V}(C), \quad W_1(C) = \frac{S(C)}{3},$ $W_2(C) = \frac{M(C)}{3}, \quad W_3(C) = \frac{4\pi}{3},$

Here $\mathcal{L}(C)$, $\mathcal{A}(C)$, and $\mathcal{V}(C)$ denote the length, area, and volume of C in dimensions 1, 2, and 3, respectively. The quantity $L(C)$ denotes the boundary length in two dimensions, $S(C)$ the surface area in three dimensions, and $M(C)$ the integral of mean curvature, defined by

$$M(C) = \int_{\partial C} m(x), dS, \quad (1.39)$$

where $m(x)$ is the mean curvature at $x \in \partial C$.

Some authors prefer to work with an equivalent family of functionals known as *intrinsic volumes*. The intrinsic volumes V_k , $k = 0, \dots, d$, are related to the Minkowski functionals by

$$b_{d-k} V_k(C) = \binom{d}{k} W_{d-k}(C). \quad (1.40)$$

In dimensions $d = 1, 2, 3$, the intrinsic volumes take the following form:

$\mathbf{d = 1}$	$V_0(C) = 1, \quad V_1(C) = \mathcal{L}(C)$
$\mathbf{d = 2}$	$V_0(C) = 1, \quad V_1(C) = \frac{\mathcal{L}(C)}{2},$ $V_2(C) = \mathcal{A}(C)$
$\mathbf{d = 3}$	$V_0(C) = 1, \quad V_1(C) = \frac{\mathcal{M}(C)}{\pi},$ $V_2(C) = \frac{\mathcal{S}(C)}{2}, \quad V_3(C) = \mathcal{V}(C).$

1.4.2 Steiner formulae

Convex geometry is closely related to mathematical morphology. In particular, Steiner formulae provide a powerful tool for expressing the volume of a convex body dilated by a ball of radius $r > 0$ in terms of its Minkowski functionals.

Definition 1.4.4. Let $A \subset \mathbb{R}^d$. The parallel set of A at distance r is defined as

$$A_{\oplus r} = A \oplus B(0, r). \quad (1.41)$$

Theorem 1.4.2 (Steiner formula). Let $C \in \mathcal{C}(\mathbb{R}^d)$ and $r > 0$. Then

$$\mu_d(C \oplus B(0, r)) = \sum_{k=0}^d \binom{d}{k} W_k(C) r^{d-k}. \quad (1.42)$$

Equivalently, in terms of intrinsic volumes,

$$\mu_d(C \oplus B(0, r)) = \sum_{k=0}^d b_{d-k} V_k(C) r^{d-k}. \quad (1.43)$$

1.4.3 Stereology and Crofton formulae

In many experimental situations, observations are obtained from images that provide only a two-dimensional representation of an inherently three-dimensional microstructure. This is notably the case in materials science, where micrographs or polished sections reveal planar cuts through a bulk material. As a consequence, one is often required to estimate geometric or topological characteristics defined in \mathbb{R}^3 from measurements performed in \mathbb{R}^2 .

A parameter is said to be *stereological* if it can be inferred from lower-dimensional observations in an unbiased manner, that is, if its expected value can be recovered from measurements performed on sections, projections, or intersections of the structure with lower-dimensional subspaces. Stereology thus provides a rigorous mathematical framework for linking measurements across dimensions.

A cornerstone of stereological theory is given by the Crofton formulae. These results relate intrinsic volumes of a convex body to mean values of intrinsic volumes of its intersections with affine subspaces of complementary dimension. In essence, Crofton formulae express global geometric quantities in terms of averages of simpler measurements performed on lower-dimensional sections.

Let $C \subset \mathbb{R}^d$ be a convex body, and let $A(d, k)$ denote the space of all k -dimensional affine subspaces of \mathbb{R}^d , endowed with the motion-invariant Haar measure $\nu_{d,k}$. For $k = 0, 1, \dots, d - 1$, the Crofton formula states that the intrinsic volume $V_{d-k}(C)$ can be expressed as

$$V_{d-k}(C) = c_{d,k} \int_{A(d,k)} V_0(C \cap E) \nu_{d,k}(dE), \quad (1.44)$$

where V_0 denotes the Euler characteristic and $c_{d,k}$ is a dimension-dependent normalization constant. In other words, intrinsic volumes can be obtained by averaging topological characteristics of intersections of C with randomly oriented affine subspaces.

More generally, Crofton-type relations take the form

$$\int_{A(d,k)} V_j(C \cap E) \nu_{d,k}(dE) = c_{d,k,j} V_{j+d-k}(C), \quad (1.45)$$

for suitable constants $c_{d,k,j}$ and admissible indices j . These identities show that quantities such as lengths, areas, surface areas, or Euler characteristics

measured on planar sections carry precise quantitative information about the three-dimensional geometry of the object.

In the practically important case $d = 3$, many classical stereological relations follow directly from Crofton formulae. For instance, the volume fraction of a phase equals the expected area fraction observed on planar sections, the surface area density is related to the mean boundary length per unit area, and curvature-related quantities can be estimated from intersection counts with test lines or planes. Crofton formulae therefore constitute the theoretical foundation of a large class of stereological estimators used in practice. When combined with assumptions such as stationarity and ergodicity of the underlying random set, they allow intrinsic volumes of random microstructures to be estimated reliably from a finite number of lower-dimensional observations. For comprehensive treatments of stereology and Crofton formulae, we refer the reader to the monographs by Stoyan, Kendall, and Mecke, and by Schneider and Weil.

1.5 Point processes

We present in this section the general theory of random point processes. A random point process \mathcal{P} is a collection of random points. Point processes can be considered as the basic ingredients of stochastic geometry. A particular role is played by Poisson point processes in the d -dimensional space \mathbb{R}^d . In section 1.5.1, we introduce a general framework for the study of point processes. We study more specifically Poisson point processes in section 1.5.2. Marked point processes are then discussed in section 1.5.3.

1.5.1 General theory

Let us first introduce a general framework for the study of point processes on locally compact topological spaces. The results of this section are technical and we will only state the most relevant ones, often without proof. We refer the reader to the reference textbooks of Weil and Schneider [46] and Stoyan *et al.* [10] for a more extensive presentation.

Random point processes as counting measures

Let E be a locally compact space with a countable topological basis. We denote by $\mathcal{B}(E)$ the Borel σ -algebra of E . Let $M(E)$ be the set of all locally

finite measures defined on E . Recall that a measure η is said to be locally finite if for all compact C in $\mathcal{K}(E)$, $\eta(C) < \infty$. For all borelian set A in $\mathcal{B}(E)$, we define the evaluation map

$$\Phi_A : M \rightarrow \mathbb{R} \cup \{\infty\}. \quad (1.46)$$

When equipped with the σ -algebra \mathcal{M} generated by all evaluation maps $\{\Phi_A, A \in \mathcal{B}(E)\}$, $M(E)$ forms a measurable space.

A class of measures of particular interest for the study of point processes is provided by the counting measures.

Definition 1.5.1. *A counting measure on E is a measure η in $M(E)$ such that for all borelian set A in $\mathcal{B}(A)$, $\eta(A) \in \mathbb{N} \cup \{\infty\}$. We denote by $N(E)$ the set of all counting measures on E .*

It can be shown that $N(E)$ is a measurable subset of $(M(E), \mathcal{M})$ [46]. We denote by \mathcal{N} the corresponding σ -algebra. A fundamental example of counting measure is given by locally finite sums of Dirac measures:

$$\eta = \sum_{k=1}^n \delta_{x_k}. \quad (1.47)$$

Another example is given by random Poisson counting measures. For all borelien set A of \mathbb{R}^d , a random Poisson counting measure follows a Poisson distribution given by

$$\eta(A) = \frac{\Theta(A)^k}{k!} \exp(-\Theta(A)), \quad (1.48)$$

where Θ is some(real) measure on the σ -algebra $\mathcal{B}(\mathbb{R}^d)$.

Point processes can be apprehended either as random sets of discrete points or as random counting measures giving the number of points contained in any domain of E . For a counting measure $\eta \in N(E)$, the support $\text{supp } \eta$ is the smallest closed set A in E such that $\eta(E/A) = 0$. The mapping $\eta \rightarrow \text{supp } \eta$ identifies a random measure to its corresponding point process. As alluded to earlier, the set of all locally finite measures on E can be equipped with a σ -algebra. This consideration enables us to define a probability law on $M(E)$.

Definition 1.5.2. A random measure X on E is a measurable map from some probability space $\{\Omega, \mathcal{A}, \mathbb{P}\}$ into the measurable space $\{M(E), \mathcal{M}\}$. The image measure \mathbb{P}_X is the distribution of X .

For a random measure X which is almost surely concentrated on $N(E)$, since $N(E)$ is a measurable subset of $M(E)$, $\text{supp } X$ is a random point process on E . Its distribution is defined for all $Y \in \mathcal{N}$ by the probabilities

$$P(Y) = \mathbb{P}\{X \in Y\} = \mathcal{P}\{\omega \in \Omega, X(\omega) \in Y\}. \quad (1.49)$$

The finite-dimensional distributions are of particular interest. They are defined for any family $\{B_1, B_2, \dots, B_k\}$ of bounded Borel sets of E to be the probabilities

$$\mathbb{P}\{X(B_1) = n_1, \dots, X(B_k) = n_k\}, \quad (1.50)$$

where n_1, \dots, n_k are positive integers.

Intensity measure

From now on, we will assume E to be the d -dimensional Euclidean space \mathbb{R}^d .

Definition 1.5.3. The intensity of the random measure X is the measure on \mathbb{R}^d defined for all borelian set A in $\mathcal{B}(\mathbb{R}^d)$ by

$$\Theta(A) = \mathbb{E}[X(A)]. \quad (1.51)$$

The intensity measure of a random point process can be seen as the equivalent of the mean of a real-valued random variable. It is of interest to consider the particular case of a stationary point process. A point process is said to be stationary if its distribution is invariant by translation. Hence, for any configuration Y in \mathcal{N} and for $x \in \mathbb{R}^d$, we have

$$\mathbb{P}\{X \in Y\} = \mathbb{P}\{X + x \in Y\}.$$

For a stationary point process, the intensity measure is necessarily translation-invariant. It implies that

$$\theta(B) = \lambda \mu_D(B), \quad (1.52)$$

where μ_D is the d -dimensional Lebesgue measure on \mathbb{R}^d and λ some positive real number.

We conclude this section by stating the Campbell theorem, a fundamental result in the theory of random measures and point processes. It shows

that expectations of random integrals with respect to a random measure are completely determined by the intensity measure. As a consequence, many first-order properties of stochastic models driven by random measures can be computed by replacing the random measure with its deterministic intensity. This theorem plays a central role in the study of Poisson random measures, stochastic geometry, and spatial stochastic models.

Theorem 1.5.1. *Let X be a random measure on E with intensity measure Θ , and let $f : E \rightarrow \mathbb{R}$ be a non-negative, measurable function. Then, we have*

$$\mathbb{E} \left[\int_E f dX \right] = \int_E f d\Theta. \quad (1.53)$$

Proof. Let X be a random measure on E with intensity measure Θ , that is,

$$\Theta(A) = \mathbb{E}[X(A)] \quad \text{for all measurable } A \subset E.$$

Step 1. Assume first that $f = \mathbf{1}_A$ for some measurable set $A \subset E$. Then

$$\int_E f dX = X(A),$$

and therefore

$$\mathbb{E} \left[\int_E f dX \right] = \mathbb{E}[X(A)] = \Theta(A) = \int_E f d\Theta.$$

Step 2. Let f be a non-negative simple function, i.e.

$$f = \sum_{i=1}^n a_i \mathbf{1}_{A_i},$$

where $a_i \geq 0$ and the A_i 's are measurable and disjoint. By linearity of the integral,

$$\int_E f dX = \sum_{i=1}^n a_i X(A_i).$$

Taking expectations and using Step 1,

$$\mathbb{E} \left[\int_E f dX \right] = \sum_{i=1}^n a_i \mathbb{E}[X(A_i)] = \sum_{i=1}^n a_i \Theta(A_i) = \int_E f d\Theta.$$

Step 3. Let f be a non-negative measurable function. There exists an increasing sequence of non-negative simple functions $(f_n)_{n \geq 1}$ such that

$$f_n \uparrow f \quad \text{pointwise.}$$

By the monotone convergence theorem,

$$\int_E f_n dX \uparrow \int_E f dX \quad \text{a.s.}$$

and

$$\int_E f_n d\Theta \uparrow \int_E f d\Theta.$$

Applying the monotone convergence theorem to expectations,

$$\mathbb{E}\left[\int_E f dX\right] = \lim_{n \rightarrow \infty} \mathbb{E}\left[\int_E f_n dX\right] = \lim_{n \rightarrow \infty} \int_E f_n d\Theta = \int_E f d\Theta.$$

□

1.5.2 Poisson point process

Definition and characterization

Definition 1.5.4. Let θ be a locally finite measure on \mathbb{R}^d . A Poisson point process on \mathbb{R}^d is a point process such that the number $N(K)$ of points contained in any compact K of \mathbb{R}^d is a Poisson random variable with parameter $\theta(K)$:

$$P\{N(K) = k\} = p_k(K) = \frac{\theta(K)^k}{k!} \exp(-\theta(K)), \quad (1.54)$$

where the intensity θ is defined by

$$\theta(K) = \int_K \theta(dx). \quad (1.55)$$

Proposition 1.5.2. The probability generating function $G_K(s)$ of the random variable $N(K)$ is

$$G_K(s) = \sum_{k=0}^{+\infty} p_k(K) s^k = \exp[\theta(K)(s-1)]. \quad (1.56)$$

Proof. By definition, the probability generating function of $N(K)$ is

$$G_K(s) = \mathbb{E}[s^{N(K)}] = \sum_{k=0}^{+\infty} p_k(K) s^k.$$

Using the expression of $p_k(K)$ for a Poisson random variable with parameter $\theta(K)$, we obtain

$$G_K(s) = \sum_{k=0}^{+\infty} \frac{\theta(K)^k}{k!} e^{-\theta(K)} s^k = e^{-\theta(K)} \sum_{k=0}^{+\infty} \frac{(\theta(K)s)^k}{k!}.$$

Recognizing the exponential series, we have

$$\sum_{k=0}^{+\infty} \frac{(\theta(K)s)^k}{k!} = \exp(\theta(K)s).$$

Therefore,

$$G_K(s) = e^{-\theta(K)} \exp(\theta(K)s) = \exp(\theta(K)(s - 1)),$$

which proves the result. \square

An important consequence of definition 1.5.4 is that for any family $\{K_i, i \in I\}$ of disjoint compact sets, the random variables $N(K_i)$ are independant. This property is referred to as *complete independance*. In many practical situations, the measure θ is proportional to the Lebesgue measure on the σ -algebra of \mathbb{R}^d . In this case, the Poisson point process is said to be *stationary* and the number $N(K)$ of points contained in a given compact K is

$$P\{N(K) = k\} = \frac{(\theta\mu_d(K))^k}{k!} \exp(-\theta\mu_d(K)), \quad (1.57)$$

μ_d being the Lebesgue measure of \mathbb{R}^d .

A Poisson point process is easily characterized by its Choquet capacity, as demonstrated below in proposition 1.5.3.

Proposition 1.5.3. *The Choquet capacity $T(K)$ of a Poisson point process is*

$$T(K) = 1 - P\{N(K) = 0\} = 1 - \exp(-\theta(K)). \quad (1.58)$$

If the process is stationary, the Choquet capacity becomes

$$T(K) = 1 - \exp(-\theta\mu_d(K)). \quad (1.59)$$

Proof. By definition, the Choquet capacity $T(K)$ of a Poisson point process is the probability that K intersects at least one point of the process. According to definition 1.5.4, we have

$$P\{N(K) > 0\} = 1 - P\{N(K) = 0\} = 1 - \exp(-\theta(K)). \quad (1.60)$$

□

For a stationary Poisson point process X , the intensity can easily be estimated from some experimental dataset by

$$\bar{\theta} = \frac{X(W)}{\mu_d(W)}, \quad (1.61)$$

where W denotes the observation window in \mathbb{R}^d . As the size of the window increases, we have $\bar{\theta} \rightarrow \theta$.

Proposition 1.5.4. *If $\mathcal{P}_1, \dots, \mathcal{P}_n$ are n independant Poisson point processes \mathcal{P}_k with respective intensities $\theta_1, \dots, \theta_n$, then the union set $\mathcal{P} = \bigcup_{k=0}^n \mathcal{P}_k$ is a Poisson point process of intensity $\theta = \sum_{k=1}^n \theta_k$.*

Proof. Let $K \subset \mathbb{R}^d$ be a compact set. For each $k = 1, \dots, n$, denote by

$$N_k(K)$$

the number of points of the Poisson point process \mathcal{P}_k contained in K . Since the point processes $\mathcal{P}_1, \dots, \mathcal{P}_n$ are independent, the random variables

$$N_1(K), \dots, N_n(K)$$

are independent Poisson random variables with respective parameters $\theta_1(K), \dots, \theta_n(K)$.

The number of points of the union process

$$\mathcal{P} = \bigcup_{k=1}^n \mathcal{P}_k$$

contained in K is

$$N(K) = \sum_{k=1}^n N_k(K).$$

The probability generating function of $N(K)$ is therefore

$$G_K(s) = \mathbb{E}[s^{N(K)}] = \prod_{k=1}^n \mathbb{E}[s^{N_k(K)}],$$

where we used the independence of the processes. By Proposition 1.5.4, the probability generating function of $N_k(K)$ is

$$\mathbb{E}[s^{N_k(K)}] = \exp(\theta_k(K)(s-1)).$$

Hence,

$$G_K(s) = \prod_{k=1}^n \exp(\theta_k(K)(s-1)) = \exp\left(\sum_{k=1}^n \theta_k(K)(s-1)\right) = \exp(\theta(K)(s-1)),$$

where

$$\theta(K) = \sum_{k=1}^n \theta_k(K).$$

This is the probability generating function of a Poisson random variable with parameter $\theta(K)$. Therefore, for every compact set $K \subset \mathbb{R}^d$, the random variable $N(K)$ is Poisson distributed with parameter $\theta(K)$, and the union process \mathcal{P} is a Poisson point process with intensity measure

$$\theta = \sum_{k=1}^n \theta_k.$$

□

Proposition 1.5.5 (Nearest-neighbor distance distribution). *Let X be a stationary Poisson point process. We define the nearest-neighbor distance distribution function Δ to be the distribution of the random distance from a typical point x of X to the nearest other point in the process. Since X is stationary, without loss of generality, it suffices to consider the case where the typical point x is the origin 0. Then, the probability distribution of Δ satisfies*

$$\mathbb{P}\{\Delta \leq r\} = 1 - e^{-\theta r^d \mu_d(B^d)},$$

where $\mu_d(B^d)$ is the Lebesgue measure of the unit ball in \mathbb{R}^d .

Proof. Let X be a stationary Poisson point process on \mathbb{R}^d with constant intensity θ . By stationarity, we may assume without loss of generality that the typical point is located at the origin 0.

The event $\{\Delta > r\}$ means that there is no other point of the process within distance r from the origin. Equivalently,

$$\{\Delta > r\} = \{X(B_r^d \setminus \{0\}) = 0\},$$

where B_r^d denotes the ball of radius r centered at the origin. Since the Poisson point process is simple, the probability of having another point exactly at the origin is zero, and we may write

$$\mathbb{P}\{\Delta > r\} = \mathbb{P}\{X(B_r^d) = 0\}.$$

Because X is a Poisson point process, the number of points in B_r^d follows a Poisson distribution with parameter

$$\theta \mu_d(B_r^d),$$

where $\mu_d(B_r^d)$ is the Lebesgue measure of B_r^d . Hence,

$$\mathbb{P}\{X(B_r^d) = 0\} = \exp(-\theta \mu_d(B_r^d)).$$

Since $\mu_d(B_r^d) = r^d \mu_d(B^d)$, where B^d is the unit ball in \mathbb{R}^d , we obtain

$$\mathbb{P}\{\Delta > r\} = \exp(-\theta r^d \mu_d(B^d)).$$

Therefore,

$$\mathbb{P}\{\Delta \leq r\} = 1 - \mathbb{P}\{\Delta > r\} = 1 - \exp(-\theta r^d \mu_d(B^d)),$$

which proves the result. \square

Simulation of a stationary Poisson point process

We describe in this paragraph the practical implementation of a stationary Poisson point process in a domain $\mathcal{D} \subset \mathbb{R}^d$. The simulation is carried out in two steps:

- First, one generates a Poisson random variable that determines the number of points located in the domain \mathcal{D} .

- Second, the corresponding number of points is sampled independently and uniformly over \mathcal{D} .

Poisson random variables can be generated from uniform random variables. In particular, if U is a random variable uniformly distributed on $[0, 1]$, then the random variable $-\ln(U)$ follows an exponential distribution, which can be used as a building block in standard algorithms for simulating Poisson random variables.

The second step of the simulation consists in generating points uniformly distributed in the domain \mathcal{D} . It is straightforward to simulate a random point uniformly distributed in the unit cube $[0, 1]^d$. For hypercubic domains, one may therefore generate points in $[0, 1]^d$ and then apply an appropriate translation and scaling to obtain points uniformly distributed in the desired domain. For more general domains, uniform sampling can be achieved using rejection sampling or approximation techniques:

- Rejection sampling consists in enclosing \mathcal{D} within a rectangular domain \mathcal{R} . Independent uniform points are generated in \mathcal{R} until a point falls inside \mathcal{D} ; this procedure is repeated until the required number of points in \mathcal{D} is obtained.
- Approximation methods consist in replacing the domain \mathcal{D} by a finite union of simple sets, such as open hypercubes, that approximate \mathcal{D} and from which uniform sampling is straightforward.

Cox-Poisson point processes

Definition 1.5.5. Let θ be a locally random finite measure on \mathbb{R}^n . A Cox-Poisson point process on \mathbb{R}^n is a point process such that the number $N(K)$ of points contained in any compact K of \mathbb{R}^n is a Poisson random variable with parameter $\theta(K)$:

$$P\{N(K) = k\} = p_k(K) = \frac{\theta(K)^k}{k!} \exp(-\theta(K)), \quad (1.62)$$

where the intensity θ is the random variable defined by

$$\theta(K) = \int_K \theta(dx). \quad (1.63)$$

Cox-Poisson point processes are an extension of Poisson point processes in the sense that for these processes, the intensity θ is a random variable.

A fundamental example of Cox point processes are Poisson point processes restricted to some random closed set. Let A be a random closed set of \mathbb{R}^n , an $\lambda > 0$. The measure

$$\theta(K) = \int_K \theta 1_A(x) dx, \quad (1.64)$$

where 1_A is the indicative function of the set A defines a Cox-Poisson point process. This Cox-Poisson point process can be seen as the restriction of a stationary Poisson point process of intensity θ to the random closed set A . Such point processes are often used in stochastic geometry to construct multiscale models. We refer the reader interested by these models to the paper of Jeulin [21].

Hard-core point processes

A hard-core point process is a point process for which the points cannot lie closer than a specified distance D . Let \mathcal{P} be an homogeneous Poisson point process with intensity θ . We can obtain a hard-core point process by thinning. Thinning consists in deleting points from the point process according to some rules. In practice, for some domain Ω , we first generate the Poisson variable N that indicates the number of points implanted in the domain. Then, we generate the points of the process sequentially. The thinning procedure occurs at each step of the simulation when a new point is added. If the nearest point is closer than the hard-core distance D , then the new implanted point is deleted.

Hard-core point processes are widely used in practical applications to model repulsion phenomena.

1.5.3 Marked point processes

A marked point process is a point process for which a characteristic is attached to each point. The notion of marked point process is fundamental in stochastic geometry and is used in many applications. We will subsequently use marked point processes to study the general Boolean model in section 1.6.

In mathematical terms, a marked point process on \mathbb{R}^d is a random sequence $\{(x_n, m_n)\}$ where the points x_n constitute a point process (unmarked) called the ground process and the m_n are the marks corresponding to the respective points. A marked point process can also be seen as a point process on $\mathbb{R} \times \mathcal{M}$, where \mathcal{M} is a locally compact space with countable base. This lead to the rigorous definition

Definition 1.5.6. *A marked point process in \mathbb{R}^d with mark space M is a simple point process X in $\mathbb{R}^d \times \mathcal{M}$ with intensity measure θ satisfying $\theta(C \times \mathcal{M}) < \infty$ for all compact set C in $\mathcal{K}(\mathbb{R}^d)$.*

The marks can be continuous or discrete variables. A marked point process is said to be stationary if its ground process is stationary. Similarly, a marked Poisson point process is simply a marked point process whose ground process is Poisson.

Definition 1.5.7. *The intensity measure of a marked point process X on $\mathbb{R}^d \times \mathcal{M}$ is*

$$\theta(B \times L) = \mathbb{E}(X(B \times L)), \quad (1.65)$$

where B is a Borel set of \mathbb{R}^d and L a measurable set of \mathcal{M} .

Intuitively, $\theta(B \times L)$ is the mean number of points in B that have their mark in L . The Campbell formula can be generalized to the case of marked point processes. Hence, let X denote a marked point process on $\mathbb{R}^d \times \mathcal{M}$. Then, we have

$$\mathbb{E}\left\{\sum_{(x,m) \in X} f(x, m)\right\} = \int f(x, m) d\Theta(x, m) \quad (1.66)$$

for any non-negative function f .

It can be shown (see for instance [46]) that the intensity of a marked point process can be decomposed in the following manner

$$d\Theta(x, m) = d\theta(x) dM_x(m), \quad (1.67)$$

where θ is the intensity measure of the ground point process and M_x is a probability measure on \mathcal{M} . We interpret M_x as the mark distribution of a point at location x .

For a stationary marked point process, for all subsets L of \mathcal{M} , $\Theta(\cdot \times L)$ is a translation-invariant measure, so that, for all Borelian set B in $\mathcal{B}(\mathbb{R}^d)$:

$$\Theta(B \times L) = \theta_L \mu_d(B), \quad (1.68)$$

where μ_d is the Lebesgue measure on \mathbb{R} . The quantity θ_L is the intensity of \mathcal{P} with respect to L , and can be interpreted as the mean number of points of \mathcal{P} per unit volume with marks in L . Obviously, if $L = \mathcal{M}$, we have $\theta_L = \theta$, where θ is the intensity of the ground point process.

Example Let X be a Poisson point process in the plane \mathbb{R}^2 with intensity θ . To each point $x_n \in X$, we associate a random mark m_n drawn from the uniform law on $[0, 1]$. All marks are drawn independently. $\{(x_n, m_n)_{x_n \in X}\}$ is a marked point process. The mark space \mathcal{M} is the σ -algebra $([0, 1], \mathcal{B}([0, 1]))$.

1.6 Germ-grain processes

1.6.1 Definition and first properties

Definition 1.6.1. Let $\Psi = \{x_n; A_n\}$ be a marked point process, where the points x_n lie in \mathbb{R}^d and the marks A_n are random compact subsets of \mathbb{R}^d . A germ-grain model can be defined from Ψ by considering the union

$$A = \bigcup_{n=1}^{\infty} (A_n \oplus x_n). \quad (1.69)$$

The points x_n are called the germs of the process and the compact sets A_n the grains of the germ-grain model.

In this section, we will restrict ourselves to the study of the Boolean model. The Boolean model is an archetypal example of germ-grain process. It is a grain model which is obtained by implanting independant random primary grains A' on the germs $\{x_k\}$ of a Poisson points process \mathcal{P} with intensity θ . Note that primary grains can possibly overlap. The resulting set A is

$$A = \bigcup_{x_k \in \mathcal{P}} A'_{x_k}, \quad (1.70)$$

where A'_{x_k} denotes the translated of the primary grain A' at point x_k :

$$A'_{x_k} = A' \oplus x_k = \{x_k + y, y \in A'\}. \quad (1.71)$$

Any shape can be used for the primary grains A' , including convex, non-convex or even non connected sets. In the literature, A' is commonly referred to as the typical grain of the model.

Definition 1.6.2. *A Boolean model is said to be stationary if the intensity of its germ process is stationary.*

First properties

Lemma 1.6.1. *Let K be a compact set of \mathbb{R}^n and A a Boolean model with primary grain A' and with intensity θ . The number $N(K)$ of primary grains hit by K follows a Poisson distribution of parameter $\mathbb{E}\{\theta(\check{A}' \oplus K)\}$:*

$$P\{N = n\} = \frac{\mathbb{E}\{\theta(\check{A}' \oplus K)\}^n}{n!} \exp(-\mathbb{E}\{\theta(\check{A}' \oplus K)\}) \quad (1.72)$$

Proof. We denote by \mathcal{P} the germ process associated to A . We can produce a thinned point process \mathcal{P}_K out of \mathcal{P} by deleting all points x_n from \mathcal{P} such that $A'_{x_n} \cap K = \emptyset$. Whether or not a given germ x_n is deleted by this procedure is independant of thinning of other germs. As a consequence, \mathcal{P}_K is an inhomogeneous Poisson point process.

We denote by θ_K the intensity of the thinned process \mathcal{P}_K . We have

$$\theta_K(x) = \theta \mathbb{P}\{A_x \cap K \neq \emptyset\}.$$

The total number of points of \mathcal{P}_K has a Poisson distribution with mean

$$\bar{N}_K = \theta \int_{\mathbb{R}^d} \mathbb{P}\{A_x \cap K \neq \emptyset\} dx.$$

Since $\mathbb{P}\{A_x \cap K \neq \emptyset\} = \mathbb{P}\{x \in \check{A}_x \oplus K\}$, we have

$$\bar{N}_K = \theta \int_{\mathbb{R}^d} \mathbb{P}\{x \in \check{A}_x \oplus K\} dx = \theta \mathbb{E}(\mu(\check{A}' \oplus K)),$$

where μ is the Lebesgues measure on \mathbb{R}^3 . This establishes formula 1.72. \square

Lemma 1.6.1 guarantees that the number of primary grains in any bounded window remains almost surely finite as long as $\mathbb{E}[\theta(A')] < \infty$. We can easily calculate the Choquet capacity of the boolean model to find

$$T(K) = 1 - \exp(-\mathbb{E}\{\theta(\check{A}' \oplus K)\}) \quad (1.73)$$

for any compact set K in $\mathcal{K}(E)$. For the stationnary case, the Choquet capacity becomes

$$T(K) = 1 - \exp(-\theta \bar{\mu}(\check{A}' \oplus K)), \quad (1.74)$$

where $\bar{\mu}(\check{A}' \oplus K)$ denotes the average Lebesgue measure (i.e the average volume) of a primary grain A' dilated by the compact set K .

We can determine the spatial law of the Boolean model by considering the Choquet capacity for the structuring element $\{x\}$. For the stationnary case, according to 1.73, we find

$$q = P\{x \in A^c\} = \exp(-\theta \bar{\mu}(\check{A}')). \quad (1.75)$$

Note that we can easily express the Choquet capacity as a function of q . Hence, we have

$$T(K) = 1 - q \frac{\bar{\mu}(A' \oplus \check{K})}{\bar{\mu}(A')}, \quad (1.76)$$

where we have used the relation $A' \oplus \check{K} = -\check{A}' \oplus K$.

Using equation 1.73, it is also possible to calculate the covariance of the Boolean model. Recall that the covariance is defined as a function of vector h of \mathbb{R}^3 by

$$C(h) = P\{x \in A, x + h \in A\}. \quad (1.77)$$

$C(h)$ is exactly the Choquet capacity for the structuring element $l_h = \{x\} \cup \{x + h\}$. Thus, we find

$$C(h) = 1 - \exp(-\mathbb{E}\{\theta(\check{A} \oplus l_h)\}). \quad (1.78)$$

For the stationnary case, the covariance yields

$$C(h) = 1 - \exp(-\theta \bar{\mu}(\check{A} \oplus l_h)). \quad (1.79)$$

Proposition 1.6.2. *If A is a Boolean model with typical grain A' and intensity θ , the covariance of A is given by*

$$C(h) = 2p - 1 + (1 - p)^2 \exp(\theta \mathbb{E}(\gamma_{A'}(h))), \quad (1.80)$$

where $\gamma_{A'}(h) = \bar{\mu}(A' \cap A'_{-h})$ is the geometrical covariogram of A' and $p = 1 - q$.

Proof. From the probabilistic definition of the covariance, we find

$$C(h) = P\{0 \in A \cap A_{-h}\} \quad (1.81)$$

$$= 1 - P\{0 \notin A\} + P\{0 \notin A_{-h}\} - P\{0 \notin A \cup A_{-h}\} \quad (1.82)$$

$$= 2p - 1 + P\{0 \notin A \cup A_{-h}\} \quad (1.83)$$

In addition, we have

$$P\{0 \notin A \cup A_{-h}\} = \exp(-\theta\bar{\mu}(A \cup A_{-h})) \quad (1.84)$$

$$= (1-p)^2 \exp(-\theta\bar{\mu}(A \cap A_{-h})), \quad (1.85)$$

since $\bar{\mu}(A \cup A_{-h}) = \bar{\mu}(A) + \bar{\mu}(A_{-h}) - \bar{\mu}(A \cap A_{-h})$. This establishes formula (1.80). \square

Examples

To illustrate the use of formula (1.80), we now consider explicit examples of typical grains A' for which the geometrical covariogram $\gamma_{A'}(h)$ can be computed analytically. These examples provide concrete expressions for the covariance function $C(h)$ of the Boolean model and highlight how the shape and size of the grains influence spatial correlations in the model. We first examine the case of circular disks in \mathbb{R}^2 , followed by spherical grains in \mathbb{R}^3 .

Proposition 1.6.3. *The geometrical covariogram of a disk with constant radius R in \mathbb{R}^2 is*

$$\gamma(R) = 2R^2 \left(\arccos\left(\frac{h}{2R}\right) - \frac{h}{2R} \sqrt{1 - \left(\frac{h}{2R}\right)^2} \right). \quad (1.86)$$

Proof. The geometrical covariogram $\gamma(h)$ of a set $A \subset \mathbb{R}^2$ is defined as the area of the intersection of A with its translation by a vector of length h :

$$\gamma(h) = \mu_2(A \cap (A + \mathbf{v})), \quad \|\mathbf{v}\| = h,$$

where μ_2 denotes the Lebesgue measure in \mathbb{R}^2 .

Let A be a disk of radius R . By rotational symmetry, the intersection area depends only on the distance h between the centers. When $h \geq 2R$, the disks do not intersect, so $\gamma(h) = 0$. For $0 \leq h \leq 2R$, the intersection forms a symmetric lens-shaped region.

The area of the lens formed by two circles of radius R with centers separated by h is given by the standard formula:

$$\mu_2(A \cap (A + \mathbf{v})) = 2R^2 \arccos\left(\frac{h}{2R}\right) - \frac{h}{2} \sqrt{4R^2 - h^2}.$$

Factoring the expression slightly differently, we can write

$$\frac{h}{2} \sqrt{4R^2 - h^2} = 2R^2 \frac{h}{2R} \sqrt{1 - \left(\frac{h}{2R}\right)^2}.$$

Substituting this into the previous formula, we obtain

$$\gamma(h) = 2R^2 \left[\arccos\left(\frac{h}{2R}\right) - \frac{h}{2R} \sqrt{1 - \left(\frac{h}{2R}\right)^2} \right],$$

which proves the proposition. \square

Proposition 1.6.4. *The geometrical covariogram of a sphere with constant radius R in \mathbb{R}^3 is*

$$\gamma(R) = \frac{4\pi R^3}{3} \left(1 - \frac{3h}{4R} + \frac{h^3}{16R^3} \right). \quad (1.87)$$

Proof. The geometrical covariogram $\gamma(h)$ of a set $A \subset \mathbb{R}^3$ is defined as the volume of the intersection of A with its translation by a vector of length h :

$$\gamma(h) = \mu_3(A \cap (A + \mathbf{v})), \quad \|\mathbf{v}\| = h,$$

where μ_3 denotes the Lebesgue measure in \mathbb{R}^3 .

Let A be a sphere of radius R centered at the origin. By rotational symmetry, the intersection volume depends only on the distance h between the centers. If $h \geq 2R$, the spheres do not intersect, so $\gamma(h) = 0$. For $0 \leq h \leq 2R$, the intersection forms a lens-shaped region (a spherical cap union).

The volume of intersection can be computed by integrating the areas of circular slices perpendicular to the line connecting the centers. If we place the centers along the x -axis at 0 and h , the intersection along $x \in [\frac{h}{2} - R, R]$

has circular cross-section of radius $\sqrt{R^2 - x^2}$. The resulting volume formula is well-known (see, e.g., standard formulas for spherical caps):

$$\gamma(h) = \frac{4\pi R^3}{3} \left(1 - \frac{3h}{4R} + \frac{h^3}{16R^3} \right).$$

Hence, the geometrical covariogram of a sphere of radius R in \mathbb{R}^3 is given by the stated expression. \square

1.6.2 Practical implementation

Simulations of random structures are generally performed on a grid of points (i.e 2D or 3D images), using primary grains based on combination of pixels. One can however rely on a completely different approach based upon level sets and implicit functions. In this approach, primary grains are described by implicit functions, which are real valued functions defined in the ambient space. The level sets of an implicit function Φ are described by an equation of the form $\Phi(x, y, z) = c$, for some constant c . A surface is described as a level set of the function Φ , most commonly the set of points for which $\Phi(x, y, z) = 0$. In this case, the points for which $\Phi(x, y, z) < 0$ correspond to the interior of the primary grain associated to the implicit function, the points for which $\Phi(x, y, z) > 0$ to its complementary and the level set $\Phi(x, y, z) = 0$ to the boundary of the primary grain. We can use any primary grain, whatever its shape, as long as we can represent it using an implicit function.

In the implicit function approach, complete simulations are generated using Boolean combinations of primary implicit functions: the union and the intersection of two objects A_1 and A_2 are defined to yield the minimum and the maximum, respectively, of their corresponding implicit functions. Thus, we have

$$\Phi(A_1 \cup A_2) = \min\{\Phi(A_1), \Phi(A_2)\}$$

and

$$\Phi(A_1 \cap A_2) = \max\{\Phi(A_1), \Phi(A_2)\}.$$

Similarly, the complementary A^c of set A is defined to be the opposite function

$$\Phi(A^c) = -\Phi(A).$$

Overall, using implicit functions to perform the simulation allows us to build complex combinations of simulations that we could not process with a pixel

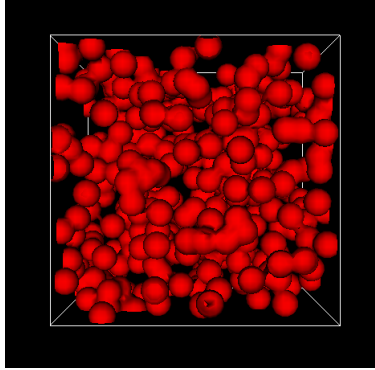


Figure 1.2: 3D Realization of a Boolean model of spheres with constant radius R and intensity θ , realized with the software vtkSim [?]. The parameters of the model are $\theta = 5 \times 10^{-2}$ and $R = 1$.

based method. Furthermore, vectorial simulations do not require a large amount of computer resources.

1.6.3 Statistical analysis for the Boolean model

In this section, we discuss statistical analysis for the Boolean model. For simplicity's sake, we restrict ourselves to the 2D and 3D cases. Our main objective is to determine the parameters of a Boolean model such as its intensity θ or its mean intrinsic volumes.

Method of densities

The method of densities (or intensities) was developed by Weil in 1984 [54] and Santaló [45] to recover the parameters of a Boolean from a given dataset. The main idea of the method is stated in proposition 1.6.5 below.

Proposition 1.6.5. *Let A be some random closed set in \mathbb{R}^d . The density of the k^{th} intrinsic volume in \mathbb{R}^d can be estimated from the dataset by relation*

$$v_k = \lim_{r \rightarrow \infty} \frac{\mathbb{E}\{V_k(A \cap B(0, r))\}}{\mu_d(B(0, r))}. \quad (1.88)$$

We recall that for $d = 2$, the intrinsic volumes are given by

$$A_A = v_2, \quad (1.89)$$

$$L_A = 2v_1, \quad (1.90)$$

$$N_A = v_0. \quad (1.91)$$

$$(1.92)$$

where A_A and L_A are the mean area and perimeter of the typical grain, respectively. N_A is called specific connectivity number. For $d = 3$, the intrinsic volumes are given by

$$V_V = v_3, \quad (1.93)$$

$$S_V = 2v_2, \quad (1.94)$$

$$M_V = \pi v_1, \quad (1.95)$$

$$N_V = v_0, \quad (1.96)$$

$$(1.97)$$

where S_V , M_V and N_V are the surface area, the specific mean curvature and the specific connectivity number, respectively.

For models with convex grains, it is possible to relate the mean values of the intrinsic volumes of the typical grain to measurements conducted on the global dataset through Miles' formulae [33]. For $d = 2$, Miles' formulae yield

$$A_A = p = 1 - \exp(-\theta \bar{A}), \quad (1.98)$$

$$L_A = \theta(1-p)\bar{S} = \theta \exp(-\theta \bar{V}), \quad (1.99)$$

$$N_A = \theta(1-p) \left(1 - \frac{\theta \bar{L}^2}{4\pi} \right). \quad (1.100)$$

For $d = 3$, Miles' formulae yield

$$V_V = p = 1 - \exp(-\theta \bar{V}), \quad (1.101)$$

$$S_V = \theta(1-p)\bar{S} = \theta \exp(-\theta \bar{V}), \quad (1.102)$$

$$M_V = \theta(1-p)\bar{S} \left(\bar{M} - \frac{\pi^2 \theta \bar{S}^2}{32} \right), \quad (1.103)$$

$$N_V = \theta(1-p) \left(1 - \frac{\theta \bar{M} \bar{S}}{4\pi} + \frac{\pi \theta^2 \bar{S}^3}{384} \right). \quad (1.104)$$

Hence, when estimates of the densities are given, the intensities of the Boolean model can easily be found. We refer the reader interested by a proof of Miles' formulae to the original paper of Miles [33] and to the book of Schneider and Weil [46].

We can illustrate the methodology for a Boolean model of disks with unknown constant radius R and intensity θ . We suppose that we dispose of a dataset, from which we can estimate a fraction area A_A and a perimeter L_A . The area of the typical grain is constant and yields $\bar{A} = \pi R^2$. Similarly, the perimeter of the typical grain yields $\bar{L} = 2\pi R$. Therefore, Miles' formulae yield

$$A_A = 1 - \exp(-\theta\pi R^2), \quad (1.105)$$

$$L_A = \theta(1 - A_A)2\pi R. \quad (1.106)$$

We can easily solve to find R and θ .

Minimum contrast method

The minimum contrast is another statistical method which can be employed to perform parameter identification for germ-grain models. It consists in trying to determine the parameters that minimize the distance between some characteristic function measured on the dataset and the corresponding function obtained either from its theoretical expression or from random realization of the model. For Boolean models, covariance is classically used in this purpose, often in combination with granulometry curves. Usually, the grain-germ models are not traceable analytically, and we have to rely on numerical methods to perform the optimization. Nelder-Mead and Levenberg-Marcquart algorithms are often used in this purpose [20]. ADD REF TO CHAP 2 HERE.

Stereological mean-value formulae

In many practical situation, we want to study the microstructure of a 3D material through 2D images that correspond to a slice of the material or to a thick section. Hence, we are left with the following question: how to relate the 2D measurements to intrinsic properties of the material?

Let A_v be a spatial stationary grain-germ process in \mathbb{R}^3 . We assume that the grains are convex. We consider the intersection of A_a of A_v with an arbitrary plane P :

$$A_a = A_v \cap P. \quad (1.107)$$

We denote (x_1, x_2, x_3) an orthonormal system of coordinates in \mathbb{R}^3 such that $x_1 \in P$ and $x_2 \in P$. For $r > 0$, we consider the disk

$$c_r = \{x = (x_1, x_2), x_1^2 + x_2^2 < r\}.$$

The number of grains hitting c_r is necessarily the same for A_v and A_a . Hence, using Steiner's formula, we find

$$\theta_v \left(\bar{V} + \frac{\pi \bar{S}r}{4} + \pi \bar{b}r^2 \right) = \theta_a \left(\bar{A} + \bar{L}r + \pi r^2 \right). \quad (1.108)$$

This equation must be valid for all $r > 0$, which proves proposition 1.6.6.

Proposition 1.6.6. *The mean value characteristics of A_v and A_a are related through relations*

$$\theta_v \bar{V} = \theta_a \bar{A} \quad (1.109)$$

$$\theta_v \frac{\pi \bar{S}}{4} = \theta_a \bar{L} \quad (1.110)$$

$$\theta_v \bar{b} = \theta_a. \quad (1.111)$$

Example Let us consider a stationary Boolean model of spheres in \mathbb{R}^3 with unknown intensity θ_v and constant radius R . The grains are balls of radius R . Experimental observations consist of planar sections of the material. The intersection of the three-dimensional Boolean model with an arbitrary plane P yields a two-dimensional Boolean model of disks, denoted by A_a .

For a sphere of radius R , the intrinsic volumes are given by

$$\bar{V} = \frac{4}{3}\pi R^3, \quad \bar{S} = 4\pi R^2, \quad \bar{b} = 1.$$

From Proposition 1.6.6, the mean value characteristics of the three-dimensional and planar models satisfy

$$\theta_v \bar{V} = \theta_a \bar{A}, \quad \theta_v \frac{\pi \bar{S}}{4} = \theta_a \bar{L}, \quad \theta_v \bar{b} = \theta_a.$$

Since $\bar{b} = 1$, the last relation implies $\theta_a = \theta_v$. Substituting the expressions of \bar{V} and \bar{S} into the first two relations yields

$$\bar{A} = \frac{4}{3}\pi R^3, \quad \bar{L} = \pi^2 R^2.$$

The planar model A_a is therefore a Boolean model of disks with intensity θ_a and mean area \bar{A} . Its area fraction A_A and perimeter density L_A satisfy

$$A_A = 1 - \exp(-\theta_a \bar{A}), \quad L_A = \theta_a \bar{L} \exp(-\theta_a \bar{A}).$$

From the first equation we obtain

$$\theta_a \bar{A} = -\ln(1 - A_A).$$

Substituting this relation into the expression of L_A gives

$$L_A = \theta_a \bar{L}(1 - A_A).$$

Replacing \bar{A} and \bar{L} by their expressions leads to the system

$$-\ln(1 - A_A) = \theta_v \frac{4}{3}\pi R^3,$$

and

$$L_A = \theta_v \pi^2 R^2 (1 - A_A).$$

Dividing the second equation by the first yields

$$\frac{L_A}{1 - A_A} = \frac{3\pi}{4R} (-\ln(1 - A_A)),$$

from which the radius is obtained as

$$R = \frac{3\pi}{4} \frac{(1 - A_A) \ln\left(\frac{1}{1 - A_A}\right)}{L_A}.$$

Finally, substituting this expression of R into the first equation gives the intensity

$$\theta_v = \frac{-\ln(1 - A_A)}{\frac{4}{3}\pi R^3}.$$

Hence, the parameters θ and R of the three-dimensional Boolean model of spheres are uniquely determined from the planar measurements A_A and L_A .

1.6.4 Notes

The Boolean model is an archetypal model of stochastic geometry. Reference textbooks on this topic include Matheron [29], Serra [47], Stoyan, Kendall and Mecke [10] and Baccelli and Blaszczyzyn [5]. We also refer the reader to the lecture notes of Jeulin [21]. For an extensive presentation, we refer the reader to the book of Schneider and Weil [46].

Regarding statistical analysis for the Boolean model, we refer the reader to the papers of Weil [54] and Molchanov [34]. Miles' formulae were derived by Miles in 1976 [33]. An introduction can be found in the book of Stoyan, Kendall and Mecke [10]. This topic is discussed more thoroughly in the book of Schneider and Weil [46].

Another topic of interest regarding the Boolean model is percolation. This topic has been studied extensively over the years. We refer the reader interested by this the percolation properties of the Boolean model to the papers of Hall [18] and Jeulin and Moreaud [24], and to the book of Torquato [50].

In materials engineering, the Boolean model has been employed to simulate a wide range of microstructures. Various examples of the application of the Boolean model in materials science are described in the paper [19] of Hermann. In 1992, Quenec'h *et al.* used the Boolean model to study the growth of WC grains in WC-Co cermets [41]. In 2001, Jeulin *et al.* relied on Poisson polyhedra to simulate the microstructure of needle-shaped gypsum crystal grains [23]. In 2003, Capasso studied the application of the Boolean model to the description of crystallisation in metals and polymers. More recently, Jean *et al.* simulated the microstructure of rubbers by considering a multiscale Cox-Boolean model [20]. Using a random walk based model, Altendorf and Jeulin developed a stochastic model for simulating 3D fiber structures [1]. Pereyga *et al.* relied on a Boolean model of random cylinders to model a random fibrous network [40].

1.7 Random Tessellations

A *tessellation* or *mosaic* is a division of the d -dimensional Euclidean space \mathbb{R}^d into polyhedra. Such geometrical patterns can be observed in many natural situations, as shown in figure 1.3. Hence, random tessellation models have been widely used in physics, materials science and chemistry.

1.7.1 General introduction

Definition 1.7.1. A tessellation in \mathbb{R}^d is a countable system \mathcal{T} of subsets satisfying the following conditions:

- $\mathcal{T} \in \mathcal{F}_{lf}(\mathbb{R}^d)$, meaning that \mathcal{T} is a locally finite system of nonempty closed sets.
- The sets $K \in \mathcal{T}$ are compact, convex and have interior points.
- The sets of \mathcal{T} cover the space,

$$\cup_{K \in \mathcal{T}} K = \mathbb{R}^d \quad (1.112)$$

- If K and K' are two sets of \mathcal{T} then their interiors are disjoint.

We denote by \mathbb{T} the set of all tessellations.

The faces of a cell C of the tessellation are the intersections of C with its supporting hyperplanes. A k -face is a face of dimension k . Among all possible k -faces, the 0-faces, or vertices, and the 1-faces, or edges, are of particular interest. The $d-1$ dimensional faces of a d -dimensional polytope will be referred to as its facets.

Proposition 1.7.1. The cells of a tessellation \mathcal{T} are convex polytopes.

Proof. Let m be a mosaic and $C \in m$. Since m is locally finite, there are only a finite number of cells, say $C_1, C_2, \dots, C_m \in m\{C\}$ that intersect C . Since a mosaic covers the whole space \mathbb{R}^d , the boundary C of C is found to be

$$C = \cup_{i=1}^m (C_i \cap C).$$

By definition, for each i between 0 and m , the relative interiors of C and C_i are disjoint. Therefore, the convex bodies C and C_i can be separated by a hyperplane H_i . More precisely, there exists an hyperplane H_i such that the closed halfspaces H_i^+ and H_i^- bounded by H_i satisfy $C \subset H_i^+$ and $C_i \subset H_i^-$. Note that this is only true because we are considering convex bodies. As a consequence, we have

$$C \subset \cap_{i=1}^m H_i^+.$$

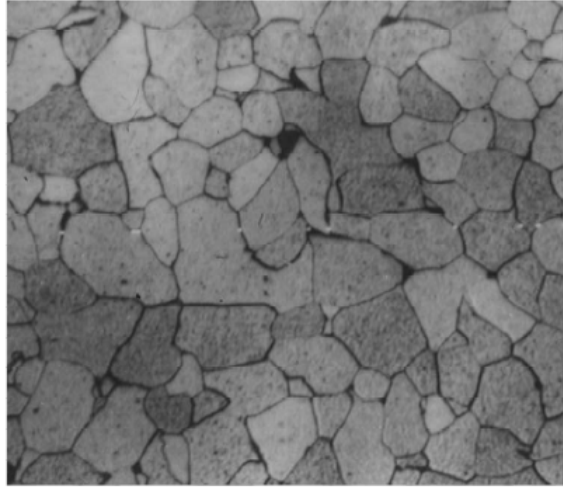


Figure 1.3: Steel polycristal microstructure

Reciprocally, let x be in $\cap_{i=1}^m H_i^+$. We suppose that $x \notin C$. Let y be an interior point of C . Necessarily, $y \in \cap_{i=1}^m H_i^+$. The line segment with end points x and y obviously contains a boundary point x' of the cell C . On the one hand, since $x \neq x'$, $x' \in \cap_{i=1}^m H_i^+$. On the other hand, $x' \in C_j$ for some $j \in \{1, \dots, m\}$. This leads to a contradiction. Therefore, if x is in $\cap_{i=1}^m H_i^+$, then x is necessarily in C . We have demonstrated that

$$C = \cap_{i=1}^m H_i^+.$$

Being compact and the finite intersection of closed halfspace, C is necessarily a convex polytope. □

General study

The general study of tessellations is rather technical, and falls beyond the scope of this introductory material. Therefore, in this chapter, we will only try to point out the general ideas behind the theory. We refer the reader interested by a more comprehensive study of general tessellation to the literature.

A fruitful idea to study general tessellations is to rely on the stochastic structures induced by the tessellation on the ambient space. For instance, if

we consider a tessellation of the plane \mathbb{R}^2 , the edges of the tessellation can be seen as a segment process. A d -dimensional tessellation \mathcal{T} also induces point processes in \mathbb{R}^d . For instance, the set of vertices of \mathcal{T} , the set of edges midpoints or the set of all cells centroids are random point processes of \mathbb{R}^d . By determining mean-value formulae for these point processes, it is possible to characterize some of the geometrical properties of \mathcal{T} . For instance, the intensity of the random point process constituted by all cells centroid correspond the mean number of cells of the tessellation per volume unit. The number $n_{d-1,d}(x)$ of edges emanating from the vertex x or the number of cells containing x are additional features of interest. Again, mean values for these quantities characterize the geometry of the tessellation. The determination of mean-values formulae for these quantites is a difficult problem, which often builds upon marked point processes theory.

Another common approach is to rely on germ-grain processes theory. Let \mathcal{T} be a tessellation of \mathbb{R}^d . If we denote by x_n the cell centers, then $\{(x_n, \mathcal{C}_n)\}$ can be seen as a germ-grain process with convex grains. We call typical cell and we note \mathcal{C}^0 the typical grain of the process. In an analogous manner, the edges midpoints with their cooresponding edges form a germ-grain process. The advantage of this approach is that one can rely on results obtained for germ-grain processes to study a tessellation \mathcal{T} .

Random tessellation in the plane

In this section, we try to illustrate the study of random mosaics for a planar tessellation. Thus, let \mathcal{T} be a tessellation on \mathbb{R}^2 . The following mean values are of particular interest to characterize \mathcal{T} :

- θ_k : Intensity of the point process of the centroids of the k -faces induced by \mathcal{T} on \mathbb{R}^2 .
- $\bar{\mathcal{A}}$: Mean area of the typical cell.
- $\bar{\mathcal{P}}$: Mean perimeter of the typical cell.
- n_{jk} : Mean number of k -faces adjacent to the typical j -faces of \mathcal{T} .

Proposition 1.7.2. *The parameters of \mathcal{T} satisfy*

$$\theta_1 = \theta_0 + \theta_2 \quad (1.113)$$

$$n_{02} = 2 + 2 \frac{\theta_2}{\theta_0}, \quad n_{20} = 2 + 2 \frac{\theta_0}{\theta_2}, \quad (1.114)$$

$$\bar{\mathcal{A}} = \frac{1}{\theta_2}, \quad \mathcal{P} = 2 \frac{\theta_1}{\theta_2} l_1, \quad (1.115)$$

$$n_{21} = n_{20}, \quad n_{01} = 3, \quad n_{10} = 2. \quad (1.116)$$

In addition, if the tessellation \mathcal{T} is normal, then we have

$$n_{02} = 3, \quad n_{20} = 6. \quad (1.117)$$

These relation are derived by considering the topological configuration of random mosaics. Some results are particularly obvious. For instance, it is clear that the number of neighbor vertices for a given edge is $n_{10} = 2$. Note that similar relations can be obtained in higher dimensions. We refer the reader to the book of Schneider and Weil [46] for a more extensive presentation of the theory and to the book of Stoyan, Kendall and Mecke [10] for the case $d = 3$.

1.7.2 Poisson tessellation models

Poisson hyperplanes

A hyperplane is a subspace of one dimension less than its ambient space. For instance, if a space is 3-dimensional then its hyperplanes are the 2-dimensional planes. An affine hyperplane is an affine subspace of codimension 1 in an affine space. In Cartesian coordinates, an affine hyperplane H can be described with a single linear equation of the following form

$$u_1 x_1 + u_2 x_2 + \cdots + u_d x_d = r, \quad (1.118)$$

where $\sum_i^d u_i^2 = 1$ and $r \in \mathbb{R}$. The vector $u = (u_1, \dots, u_d)^T$ is orthogonal to H and unitary. We denote by \mathcal{A} the set of all affine hyperplanes of \mathbb{R}^d . An hyperplane is completely characterized by u and r , and can thus be considered as the image of these quantities by the application

$$\Psi : (u, r) \in \frac{1}{2}\mathbb{S} \times \mathbb{R} \rightarrow \mathcal{A} \ni H(u, r), \quad (1.119)$$

where

$$H(u, r) = \{x \in \mathbb{R}^d, u_1 x_1 + u_2 x_2 + \cdots + u_d x_d = r\}. \quad (1.120)$$

and \mathbb{S} is the unit semi-sphere of \mathbb{R}^d .

Definition 1.7.2. Let \mathcal{P} be a Poisson point process in $\frac{1}{2}\mathbb{S} \times \mathbb{R}$ with intensity $\theta(d\mathbf{u})dx$, where θ is a positive Radom measure on the semi-sphere $\frac{1}{2}\mathbb{S}$. The image of \mathcal{P} by application Ψ is the random closed set \mathcal{H} called Poisson hyperplanes network.

Remark One could have thought of relying on a classical Boolean model with lines as grains to construct Poisson hyperplanes. The problem with this approach is that lines are not bounded and therefore not compact.

Theorem 1.7.3. Let K be a compact set of \mathbb{R}^d . The number of hyperplanes hit by K is a Poisson random variable with intensity

$$\theta(K) = \int_{\frac{1}{2}\mathbb{S}} \nu_1(K|_{\mathbf{u}})\theta(d\mathbf{u}). \quad (1.121)$$

In this expression, $\nu_1(K|_{\mathbf{u}})$ denotes the total length of the orthogonal projection of K on direction \mathbf{u} .

Proof. By construction, the intersection of \mathcal{T} with every line with unit support vector \mathbf{u} is a Poisson point process with intensity $\theta(d\mathbf{u})$. Hence, the number of hyperplanes hit by K for a given direction \mathbf{u} is $\nu_1(K|_{\mathbf{u}})\theta(d\mathbf{u})$. \square

Using theorem 1.7.3, we can easily prove the following proposition.

Proposition 1.7.4. The Choquet capacity of a Poisson hyperplanes network H is given for all compact sets K in \mathbb{R}^d by

$$T(K) = 1 - \exp \left[- \int_{\frac{1}{2}\mathbb{S}} \nu_1(K|_{\mathbf{u}})\theta(d\mathbf{u}) \right]. \quad (1.122)$$

Poisson lines tessellations

Poisson hyperplanes can be used to produce random tessellations. In this section, we restrict ourselves to the plane \mathbb{R}^2 .

Definition 1.7.3. Let \mathcal{L} be a planar motion-invariant line process of intensity θ . \mathcal{L} induces a stationary tessellation on \mathbb{R}^2 , called Poisson line tessellation. The line intersections form the vertices of the tessellation, and segments of line with vertices at both endpoints form the edges.

To characterize the tessellation, we introduce the quantity

$$\rho = \frac{2\theta}{\pi}, \quad (1.123)$$

which corresponds to the mean number of lines intersected by a test line segment of unit length. Let g be a fixed line of \mathcal{L} . Then, the intensity of the point process of intersection points on g is given by ρ . As a consequence, the mean edge length is

$$l_1 = \frac{1}{\rho} \quad (1.124)$$

With probability one, there are no triplets of lines that meet at the same vertex. Hence, we have

$$n_{02} = 4 \quad (1.125)$$

almost surely. Therefore, using proposition, we find

$$\theta_0 = \frac{\pi\rho^2}{4}, \quad (1.126)$$

$$\theta_1 = \frac{\pi\rho^2}{2}, \quad (1.127)$$

$$\theta_2 = \frac{\pi\rho^2}{4}. \quad (1.128)$$

Definition 1.7.4. *The typical cell of the Poisson hyperplane tessellation is called Poisson polygon.*

The first moments of Poisson polygon can easily be calculated with proposition, to find

$$\bar{\mathcal{A}} = \frac{4}{\pi\rho^2}, \quad (1.129)$$

$$\bar{\mathcal{L}} = \frac{4}{\rho}. \quad (1.130)$$

1.7.3 Poisson-Voronoi tessellations

We present in this section the Poisson-Voronoi tessellation model. This model has been studied extensively and is a classical model in stochastic geometry.



Figure 1.4: Simulations of WC-Co cermet microstructures using Poisson polygons. This figure is taken from the study [41] of Quenec'h *et al.*

Definition

Let Ω denote a given volume in \mathbb{R}^3 . A Voronoï tessellation is a tessellation built from a Poisson point process \mathcal{P} in the space \mathbb{R}^3 . Every point x of \mathbb{R}^3 is associated to the class \mathcal{C}_i containing all points of \mathbb{R}^3 closer from the point x_i of \mathcal{P} than from any other point of \mathcal{P} . Hence, the classes $C_i, i = 1, \dots, N$ are defined by

$$C_i = \left\{ y \in \mathbb{R}^3, \forall j \neq i, \|x_i - y\| \leq \|x_j - y\| \right\}. \quad (1.131)$$

It can be shown that with probability one, Voronoï tessellations are normal and face-to-face. Voronoï tessellations are characterized by one single parameter, namely the intensity of the underlying point process. Thus, according to proposition, for a Voronoï tessellation in the plane, we have

$$\theta_2 = \theta, \quad (1.132)$$

$$\theta_0 = 2\theta, \quad (1.133)$$

$$\theta_1 = 3\theta, \quad (1.134)$$

where θ_0 , θ_1 and θ_2 denote the intensities of the point processes constituted by the vertices, the edges center and the cell centers, respectively. Similarly,

the mean area of a cell of the tessellation is

$$\bar{\mathcal{A}} = \frac{1}{\theta}. \quad (1.135)$$

These relations can be generalized for $d > 2$.

Johnson-Mehl Tessellations

Johnson-Mehl tessellations can be seen as a sequential version of the Voronoï model, where the Poisson points are implanted sequentially with time. All classes grow then isotropically with the same rate, and the growth of crystal boundaries is stopped when they meet. All Poisson points falling in an existing crystal are removed. From a mathematical perspective, a Johnson-Mehl tessellation is constructed from a sequential Poisson point process where the points $x_i, i = 1, \dots, N$ are implanted sequentially at a time $t_i, i = 1, \dots, N$. The classes $C_i, i = 1, \dots, N$ corresponding to the points $x_i, i = 1, \dots, N$ are defined by

$$C_i = \left\{ y \in \mathbb{R}^3, \forall j \neq i, t_i + \frac{\|x_i - y\|}{v} \leq t_j + \frac{\|x_j - y\|}{v} \right\}. \quad (1.136)$$

Note that when all times are set to zero, we recover the classical Poisson-Voronoï tessellation model.

Notes

Random tessellations constitute an active topic in stochastic geometry. Reference textbooks on this topic include Matheron [29], Stoyan, Kendall and Mecke [10]. For an extensive presentation, we refer the reader to the book of Schneider and Weil [46], where a proof is given for almost all results. The mean-value relationships given in section 1.7.1 are mostly due to the studies of Mecke [30] and Møller [35].

Poisson hyperplanes tessellations and Poisson polyhedra have been extensively studied by Matheron [29], Serra [47] and Miles [32]. We also refer the reader to the paper [31] of Mecke.

The Voronoï tessellation is a classical model in stochastic geometry. A general description of Poisson-Voronoï tessellations in \mathbb{R}^d can be found in Møller [35, 37]. The Johnson-Mehl tessellation model was introduced by Johnson and Mehl to describe crystallization processes [26, 4, 17]. Their model can be seen as a variation of the Voronoï model. The paper [36] of Møller provides a unified exposition of Random Johnson-Mehl tessellations.

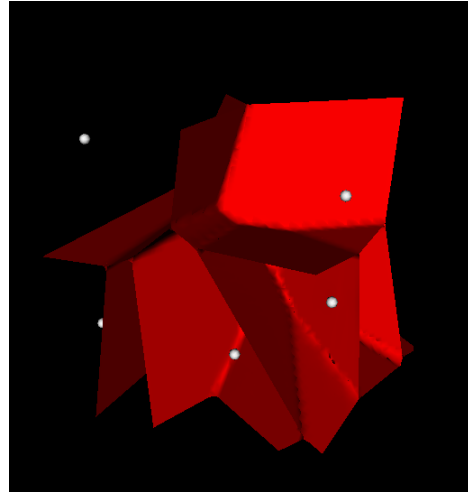


Figure 1.5: Voronoï tessellation in \mathbb{R}^3 . The simulation has been obtained with the software VtkSim [?]. The center of the Voronoï cells are represented in grey.

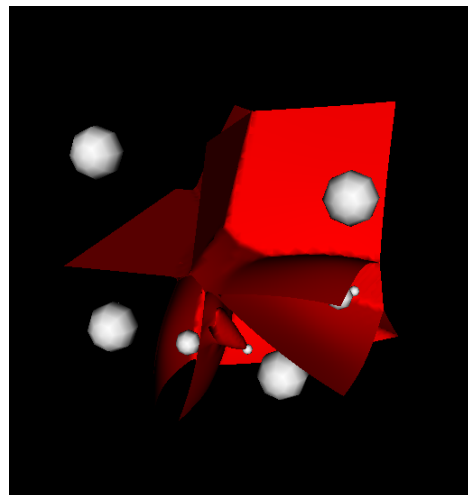


Figure 1.6: Voronoï tessellation in \mathbb{R}^3 . The simulation has been obtained with the software VtkSim [?]. The center of the tessellation cells are represented in grey. The first germs are represented with larger radii.

Chapter 2

Morphological models in materials science

Most materials encountered in contemporary life and industrial applications are heterogeneous and characterized by complex internal microstructures. These microstructures play a central role in determining their macroscopic physical and mechanical properties [50]. As a result, accurately modeling and reproducing material microstructures is a crucial step toward understanding and predicting material behavior at larger scales.

In this context, the generation of random microstructures that faithfully reproduce the geometrical characteristics of real materials has attracted considerable attention [9, 39, 25, 50, 42, 43]. Such synthetic microstructures provide a powerful framework for investigating the physical and mechanical properties of heterogeneous materials through large-scale numerical simulations [1, 40, 24, 38, 27]. By enabling controlled variations of geometric features, this approach offers valuable insights into the relationship between microstructure and macroscopic material properties, with strong potential for both fundamental research and industrial applications.

This chapter presents selected research topics related to the simulation of material microstructures and, more broadly, to morphological modeling. Section 2.1 focuses on the development of microstructure models for a copper coating produced by the cold spray process, with the aim of investigating how the substrate microstructure influences electrical conduction at the macroscopic scale. We then address in section 2.2 a fundamental issue common to morphological models: once a model has been defined, how can its parameters be selected in a statistically consistent manner? To tackle this problem,

we present an approach based on Markov Chain Monte Carlo algorithms, which provides an effective framework for parameter estimation in complex microstructural models. Finally, we discuss in section 2.3 an approach based on the resolution of the Eikonal equation to efficiently generate random tessellations.

2.1 Microstructure modelling with morphological models

We present in this section the development of a morphological model used for studying the electrical characteristics of a bi-phased coating produced through thermal spraying [6, 2, 12]. This coating is specifically designed to shield recent commercial aircraft bodies from lightning strikes by providing a conductive surface that can effectively dissipate electrical charges. To our knowledge, this study represents one of the earliest efforts to model the electrical properties of coldspray deposits based on their microstructure. This research work was carried out in collaboration with Vincent Bortolussi, Michel Jeandin (Centre des matériaux, Mines Paris), François Willot and Matthieu Faessel (Centre de morphologie mathématique, Mines Paris) and was partially funded by a grant from Air Force Office of Scientific Research (AFOSR). It led to several publications related to the morphological model itself [7] and to its exploitation to study the electric conductivity of coldspray coatings [8].

2.1.1 Context

Modern commercial aircraft are constructed using carbon fiber-reinforced polymers, which provide excellent mechanical properties while being significantly lighter than traditional aluminum alloys. However, the polymer matrix in these materials is generally highly electrically insulating, which poses security concerns in the event of lightning strikes. Advanced aerospace composites are typically fabricated using a matrix of PEEK (Poly-Ether-Ether-Ketone), a thermoplastic polymer that offers good mechanical and thermal properties while being an excellent insulator. To address the need for electrical charge dissipation in the event of lightning strikes, a layer of copper mesh is typically applied to the composite body. Copper is an easily machinable and corrosion-resistant electrical conductor with low electrical resistivity.

2.1.2 Experimental data

To simplify the manufacturing and assembly of copper meshing, a new coating method was developed, which relies on copper powder being thermally sprayed onto composite parts. Specifically, an adherent and electrically conductive layer is achieved by using a powder mixture containing 80% volumetric of spherical copper powder (10-35 microns) and 20% of irregular PEEK particles (35-65 microns). The mixture is applied using the cold-gas dynamic spraying or “cold spray” process.

In our work, we relied on microscopic images of the coating to study the resulting microstructure. Prior to observation, the cold spray coatings underwent cross-sectioning and polishing. To do this, the coating samples were cut in two directions: along the spraying path and orthogonal to it. Unfortunately, cutting and polishing caused debonding of the copper particles due to poor mechanical anchorage in the matrix. This resulted in dark holes at the surface. It should be noted that manual polishing can have a significant impact on the debonding phenomenon. To counteract this, the samples were metallized with a layer of Gold-Palladium that was only 2 nm thick, using a Cressington sputter coater. This was a crucial step as the layer modified the color of the PEEK matrix, greatly enhancing the color gradient between phases. To observe the cross-sections, we used a Leica optical microscope at $\times 20$ magnification in bright field. The microscope had a resolution of 0.2428 microns per pixel. We selected this observation scale to obtain a representative fraction of copper while also highlighting PEEK interstices.

The microstructure of the cold spray coating can be observed in Fig. 2.1, where yellow copper particles are embedded in a grey PEEK matrix that contains dark footprints. The matrix is made up of irregular PEEK particles that become highly deformed upon high speed impact, resulting in a dense structure with no visible pores at this scale. The copper particles deform only upon impact with each other, resulting in limited plastic strain and forming a network of copper clusters. In typical cold spraying of metal particles onto a metal substrate, chemical bonding and inter-diffusion occur at the interfaces between particles and substrate. However, in our case, optical observation at a larger scale highlights thin PEEK layers are lying between deformed copper particles, as shown in Fig. 2.1. These interstices prevent direct contact between copper particles and are filled with electrically insulating PEEK, allegedly increasing resistivity and thus lowering the conductivity of the coating. Fig. 2.2 is an optical microscope cross-section of

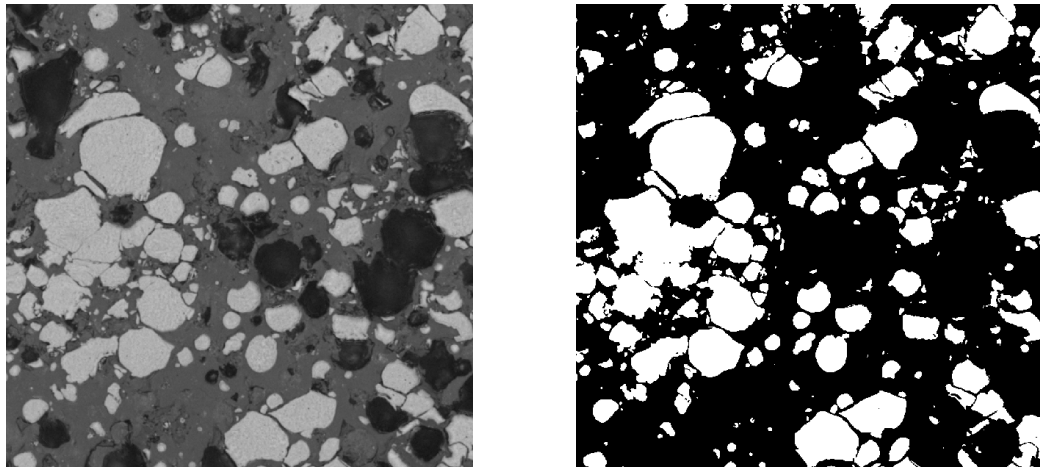


Figure 2.1: Original image and corresponding segmentation mask.

the coating microstructure with debonded particles appearing in black. The image comprises 2560×1920 pixels representing a surface area of $620 \times 476 \mu\text{m}^2$. Fig. 2.2 is a magnified optical microscope cross-section of the coating's microstructure, with the image comprising 2560×1920 pixels representing a surface area of $248 \times 186 \mu\text{m}^2$.

The first step of our study consisted in developing a segmentation algorithm of the experimental images in order to identify the copper particles within the microstructures as well as the interstices separating these particles. We refer the reader seeking additional details on the segmentation algorithm to the original article [7]. Segmentation results are displayed in Fig. 2.1. Overall, we performed the segmentation of $K = 13$ large images of the microstructure, and we used these images to compute experimental covariance and granulometry curves that characterize the coating microstructure.

2.1.3 Morphological model

We present in this section the multi-scale morphological model [22] developed for describing the microstructure geometry. To construct the model, we make the assumption that the microstructure consists of copper spheres embedded in a PEEK matrix, separated by thin PEEK interstices. The covariance, copper fraction, granulometry, and interstice thickness are measured on 2D slices of the coating. Therefore, the parameters of the 3D model need to be inferred from this 2D information. The final two-scale model is based on a

two-step simulation process:

1. The first step of the simulation process corresponds to the generation of a Boolean model of spheres with intensity θ . The radii of the spheres follow a Gamma distribution law with parameters λ and a . This first scale of the model intends to represent the set of copper particles, which form aggregates due to interpenetration.
2. The second step involves intersticce implantation based on a modified Johnson-Mehl tessellation. This two-scale model provides a representation of the 3D microstructure of the coating based on the 2D information obtained from the slices.

Aggregates simulation We assume that the copper particles aggregates can be represented by a Boolean model of spheres and that the distribution of the radii of the spheres is described by a Gamma law. The probability density function of the Gamma law is given by

$$p(r, \lambda, a) = \frac{r^{a-1}}{\Gamma(a)\lambda^a} \exp\left(-\frac{r}{\lambda}\right), \quad (2.1)$$

where Γ denotes the Gamma function. The average radius of the typical sphere is $a\lambda$. Its variance is $a\lambda^2$. The average surface of the typical grain is

$$S_v = \int_0^{+\infty} \frac{4\pi r^{a+1}}{\Gamma(a)\lambda^a} \exp\left(-\frac{r}{\lambda}\right) dr = 4\pi\lambda^2 a(a+1). \quad (2.2)$$

Similarly, its average volume is

$$V_v = \int_0^{+\infty} \frac{4\pi r^{a+2}}{3\Gamma(a)\lambda^a} \exp\left(-\frac{r}{\lambda}\right) dr = \frac{4\pi}{3}\lambda^3 a(a+1)(a+2). \quad (2.3)$$

To determine the 3D parameters of the model using 2D measurements, we use the stereological formulae

$$\theta_3 V_v = \theta_2 \bar{A}, \quad \theta_3 S_v = \frac{4}{\pi} \theta_2 \bar{L}, \quad (2.4)$$

where \bar{A} is the mean area of the sliced spheres, \bar{L} their perimeter, θ_3 the 3-dimensional intensity parameter and θ_2 the intensity of the disk process on sections. We need to relate the 2D measurements to the parameters of

the Boolean model. To that end, we rely on Miles' formulae [32, 10, 46], discussed in chapter 1:

$$A_a = 1 - e^{(-\theta_2 \bar{A})}, \quad L_a = \theta_2 \bar{L}(1 - A_a), \quad (2.5)$$

where A_a is the mean surface fraction of copper on segmented images and L_a is the mean perimeter of the copper phase on segmented images divided by the total surface. Using Miles' formulae in conjunction with stereological formulae [10, 46], we find, for the Boolean model

$$\mathcal{A}_a = 1 - \exp(-\theta V_v), \quad \mathcal{L}_a = \theta \frac{\pi}{4} S_v \exp(-\theta V_v). \quad (2.6)$$

Overall, there are three unknowns in the model, namely the intensity θ of the Boolean model and the parameters a and λ of the Gamma distribution. Hence, we can express all parameters as functions of a . Using (2.6), we find

$$\theta = -\frac{3}{4\pi\lambda^3 a(a+1)(a+2)} \ln(1 - \mathcal{A}_a), \quad (2.7)$$

and

$$\lambda = -\frac{3\pi}{4(a+2)\mathcal{L}_a} (1 - \mathcal{A}_a) \ln(1 - \mathcal{A}_a). \quad (2.8)$$

To determine the parameters of the stochastic model, we rely on a maximum likelihood approach to find the parameters that minimize the least-square distance between the covariance of the simulated microstructure and the covariance that is measured on the available experimental dataset. However \mathcal{L}_a is highly influenced by interconnection between particles. As many particles remain in contact due to interstices segmentation, computing θ only from λ and a provides a more robust algorithm.

Interstices implantation To simulate the interstices between the particles of the same aggregate, we use a random Johnson-Mehl tessellations restricted to each aggregate, or connected component of the first scale of the microstructure. For each connected aggregate \mathcal{A} of the first scale of the simulation, we consider n germs and we simulate a random number ζ_n according to an exponential law with some mean k , which will parameterize the thickness of the boundary between cells. The cells of the tessellation are then defined by

$$C_i = \left\{ y \in \mathcal{A}, \forall j \neq i, t_i + \frac{\|x_i - y\|_G}{v} + \zeta_i \leq t_j + \frac{\|x_j - y\|_G}{v} \right\}. \quad (2.9)$$

In this relation, $\|\cdot\|_G$ denotes the geodesic distance with respect to the realization of the Boolean model and t_i is the implantation time of the i -th grain. With this definition, we note that some points of the aggregates do not belong to any class of the Johnson-Mehl tessellation. We consider that these points form the interstices between the grains of the microstructure.

A significant question remains, which is how to select the initial germs of the tessellation and the germination times. While selecting the germs, our aim is to preserve the geometrical shape of the grains of the microstructure. Hence, we seek to set the germs in the center of connected components to simulate a granular microstructure. To the end, we rely on the *h-maxima* [47] of the distance function to generate the germs. The *h-maxima* of the distance function form connected components. For each component, we select its barycentre to be the location of a germ. The threshold for the *h-maxima* is selected after an optimization procedure that aims at minimizing the distance between the granulometries. For each germ n , we denote by d_n the value of the Euclidean distance function at the location of the germ. The germination time associated to germ n is defined to be

$$t_n = (\max_m d_m) - d_n. \quad (2.10)$$

With this choice of germination time, the cells border of bigger spheres are kept close from the edges of the spheres and we are able to preserve the geometrical shape of the grains constituting the microstructure.

2.1.4 Results and discussions

To assess the relevance of the proposed stochastic model, we compared several morphological descriptors between experimental and simulated microstructures. These descriptors include the covariance function, the granulometry, and the interstice thickness distribution. The combined use of covariance and granulometry is common in morphological modeling, as the granulometry characterizes object size distributions while the covariance provides second-order statistics related to spatial organization and scale superposition. The interstice thickness distribution is a key feature specific to the present study. Owing to the strong electrical resistivity contrast between copper and PEEK, even small variations in interstice size can significantly affect the macroscopic electrical conductivity of the coating.

Figure 2.3 presents a two-dimensional slice of a simulated microstructure obtained using parameters estimated through the maximum likelihood

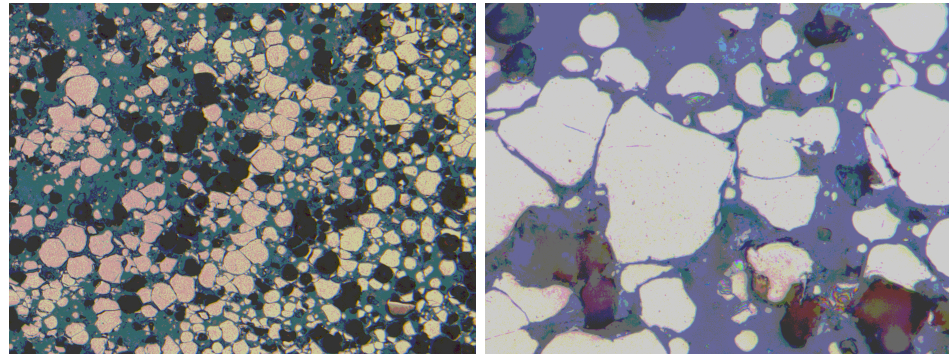


Figure 2.2: Optical microscope cross-section of the coating (2560×1920 pixels representing a surface area of $248 \times 186 \mu\text{m}^2$).

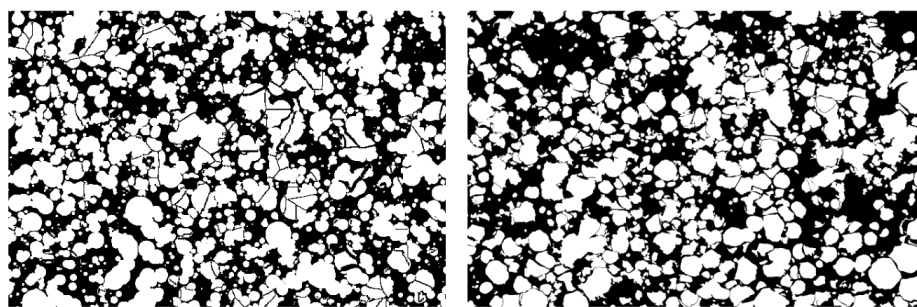


Figure 2.3: Simulation of the microstructure with the optimized parameters.

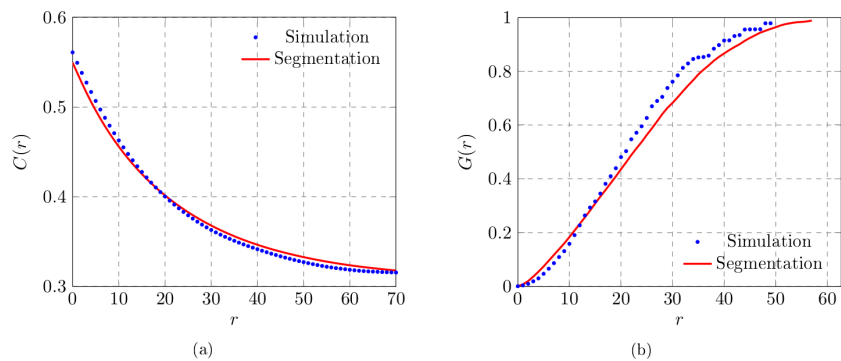


Figure 2.4: Simulated and experimental microstructures comparisons between covariances (a) and granulometries (b).

Table 2.1: Model parameters.

A_a	$\theta (\mu\text{m}^{-3})$	$\lambda (\mu\text{m})$	a	$k (\mu\text{m})$	$h (\mu\text{m})$	p
63%	4.8×10^{-3}	2.3	0.8	1.2	7.26	0.5

procedure. The corresponding parameter values are reported in Table 2.1, where A_a denotes the copper surface fraction measured on segmented images, θ the intensity of the Poisson point process, λ and a the parameters of the Gamma distribution governing particle radii, h the threshold used to extract distance-function maxima, and p the proportion of selected maxima.

Comparisons between experimental and simulated covariances and granulometries are shown in Fig. 2.4. We can note that a small discrepancy, on the order of 0.01, appears in the covariance for distances between 10 μm and 40 μm . This difference is attributed to the presence of a few relatively large polymer-rich regions devoid of copper particles, which can be observed in Fig. 2.2.

2.1.5 Conclusion

In this section, we developed a two-scale stochastic morphological model to describe the three-dimensional microstructure of cold spray copper-PEEK coatings from two-dimensional experimental observations. The model combines a Boolean model of spheres with Gamma-distributed radii to represent copper particle aggregates, and a modified Johnson-Mehl tessellation to account for the thin PEEK interstices separating particles within aggregates. Model parameters were inferred from stereological relations and optimized by matching covariance and granulometry descriptors measured on segmented experimental images.

Comparisons between simulated and experimental microstructures show good agreement in terms of covariance and granulometry, indicating that the proposed model successfully captures both the spatial organization and the size distribution of copper particles. The inclusion of interstice implantation proves essential for reproducing realistic microstructural features that strongly influence electrical transport properties. This morphological framework therefore provides a consistent and physically grounded basis for subsequent numerical simulations of the effective electrical conductivity of cold spray coatings.

2.2 Parameters estimation in morphological models

We presented in the previous section a morphological model designed to reproduce the microstructure of cold-spray-deposited materials from experimental imaging data. Morphological models typically rely on a set of parameters, denoted by Θ , which must be carefully selected to ensure consistency with experimental observations. A common strategy for determining these parameters consists in minimizing an objective function, usually defined as a measure of discrepancy between quantities obtained from numerical simulations and those measured experimentally. Numerous approaches have been proposed in the literature to address this optimization problem.

A classical technique involves minimizing the objective function using a gradient descent algorithm. Gradient descent methods are first-order iterative optimization algorithms that aim to locate a local minimum of a differentiable function by iteratively moving in the direction of the negative gradient in parameter space. While these algorithms are highly effective for strongly convex problems, their application to morphological models raises several difficulties. First, the gradient of the objective function is often analytically intractable and must be approximated using finite-difference schemes. This approximation requires at least $D + 1$ evaluations of the objective function, where D denotes the dimension of the parameter space, and is further affected by the intrinsic statistical variability of morphological models, which typically leads to noisy gradient estimates. Second, the objective function is generally non-convex, so gradient-based methods are prone to converging to local minima.

Several alternatives to gradient descent have been proposed in the literature. In particular, in [52, 53, 51, 15], the authors advocate the use of the Nelder-Mead algorithm, a heuristic optimization method for locating extrema of an objective function in a multidimensional space. As a direct search method based solely on iterative evaluations of the objective function, it is well suited to situations in which gradient information is unavailable or unreliable.

In this section, we address the relatively underexplored problem of parameter estimation for morphological models. We introduce an approach based on a Bayesian formulation of the problem, originally proposed in [16]. This framework yields a posterior distribution for the model parameters condi-

tioned on the experimental observations. Samples from this posterior distribution are generated using a Markov Chain Monte Carlo (MCMC) algorithm. Compared to deterministic optimization methods, this approach offers several advantages: in particular, MCMC sampling provides a faithful representation of the posterior distribution, enables the identification of correlations between model parameters, and allows for a quantitative assessment of their respective influences.

2.2.1 Problem statement

Let us consider a set of previously segmented experimental images of a material's microstructure, which we denote as the observations \mathcal{O} . The geometry of the microstructure can be characterized by computing several statistical features, including the covariance, the granulometry, or the granulometry of the complementary image.

The covariance of a random set A was defined in Chapter 1 as the function C_A on $\mathbb{R}^d \times \mathbb{R}^d$ given by

$$C_A(x, x + h) = P(x \in A, x + h \in A), \quad (2.11)$$

where $h \in \mathbb{R}^d$. For a stationary random set, the covariance depends only on the displacement h :

$$C_A(x, x + h) = C_A(h). \quad (2.12)$$

Next, we consider the granulometry of the microstructure. Let K be a convex set, and let $(K_\lambda, \lambda > 0)$ denote a family of scaled structuring elements, where $K_\lambda = \lambda K$. For any closed set $A \subset \mathbb{R}^d$, the operator

$$\Phi_\lambda(A) = (A \ominus \check{K}_\lambda) \oplus K_\lambda, \quad (2.13)$$

defines a granulometry, where \ominus denotes morphological erosion and \oplus denotes morphological dilation.

The granulometry obtained by openings characterizes the size distribution of the elements of A . Specifically, for distinct values of λ , one can record the volume fraction of the residual set

$$A \setminus \Phi_\lambda(A),$$

to quantify the size distribution. In this work, granulometry measurements are computed both on the set A and on its complement A^c .

In the remainder of this section, we denote by $m_{\mathcal{O}}$ the statistical measurements derived from the observations and by m_{Θ} those obtained from simulated microstructures. The model parameters Θ are typically chosen to minimize the discrepancy between $m_{\mathcal{O}}$ and m_{Θ} . This parameter estimation can be formulated as the following constrained optimization problem:

$$\hat{\Theta} := \arg \min_{\Theta} \|m_{\mathcal{O}} - m_{\Theta}\|_2^2 \quad \text{subject to } \Theta \in \mathcal{D}, \quad (2.14)$$

where \mathcal{D} denotes the set of admissible model parameters.

2.2.2 Bayesian formulation

Starting from measurements obtained from a morphological model and from experimental observations of the studied microstructure, we use a Bayesian approach to determine the parameters of the model. The likelihood that the observations were obtained with the set of parameters Θ can be defined as follows:

$$p(\mathcal{O}|\Theta) = \frac{1}{\sqrt{2\pi|\Lambda|}} \exp\left(-\frac{1}{2}(m_{\mathcal{O}} - m_{\Theta})^T \Lambda^{-1} (m_{\mathcal{O}} - m_{\Theta})\right), \quad (2.15)$$

In Eq. (2.15), we usually consider a diagonal covariance matrix Λ and we assign a weight to the parameters corresponding to their respective importance. The arbitrary choice of a Gaussian distribution is motivated by its simplicity, but other distributions could potentially be considered for the likelihood.

We resort to physical considerations to define a prior distribution on the parameters Θ . Usually, we are able to define a range of variation for all parameters of the model based on their physical validity:

$$\Theta_{\min} \preceq \Theta \preceq \Theta_{\max}, \quad (2.16)$$

where \preceq is a component-wise inequality. We simply consider a uniform distribution between the lower and the upper bound for each parameter as prior distribution:

$$p(\Theta) := \mathcal{U}_{\Theta_{\min}, \Theta_{\max}}. \quad (2.17)$$

Thanks to Bayes formula, we obtain an expression for the posterior distribution of the parameters Θ knowing the observations:

$$p(\Theta|\mathcal{O})p(\mathcal{O}) = p(\mathcal{O}|\Theta)p(\Theta). \quad (2.18)$$

Since the (unknown) probability law for the observation is independent from Θ , the posterior distribution is proportional to the product of the likelihood and of the prior distribution:

$$p(\Theta|\mathcal{O}) \propto p(\mathcal{O}|\Theta)p(\Theta). \quad (2.19)$$

The problem of the model parameterization becomes the determination of a set of parameters maximizing the posterior probability $p(\Theta|\mathcal{O})$:

$$\hat{\Theta} = \operatorname{argmax}_{\Theta} p(\Theta|\mathcal{O}). \quad (2.20)$$

2.2.3 Sampling from the posterior distribution

A question now arises, which is how to solve the optimization problem from Eq. (2.20) in practice? An obvious solution could be to use a gradient ascent algorithm to find local maxima in the parameters space. In this section, we propose a distinct approach consisting in using a Monte Carlo Markov Chains (MCMC) algorithm to generate samples from the posterior distribution [44, 3]. This approach offers several benefits compared to gradient ascent. Computing the gradient of the measurements with respect to the parameters is often challenging due to two primary factors. Firstly, there is usually no readily available analytical formula to calculate the gradient. Secondly, the function m_{Θ} is a stochastic function dependent on the parameter set Θ , making it difficult to estimate the gradient using a finite difference scheme. Moreover, the MCMC approach possesses an additional advantage as it enables the generation of samples that accurately represent the posterior distribution. This capability allows for the capture of noteworthy characteristics of the microstructure, including parameter correlations and characteristic ranges of parameter variation. The algorithm that we propose works as follows:

- *Initialization:* At initialization, we first generate a set of parameters from the prior distribution:

$$\Theta_1 \sim \mathcal{U}_{\Theta_{\min}, \Theta_{\max}}. \quad (2.21)$$

- *n-th iteration:* At each iteration, we repeat the following steps:

1. *Parameters sampling* we generate a set of parameters $\hat{\Theta}$ from the current state Θ_n according to a proposal distribution q :

$$\hat{\Theta} \sim q(\hat{\Theta}|\Theta_n) \quad (2.22)$$

2. *Simulation* We compute a simulation of the morphological model with this set of parameters, and perform measurements on the computed microstructure. The measurements $m_{\hat{\Theta}}$ are used to compute the posterior distribution, up to the constant factor $p(\mathcal{O})$:

$$p(\hat{\Theta}|\mathcal{O}) \propto p(\mathcal{O}|\hat{\Theta})p(\hat{\Theta}). \quad (2.23)$$

3. *Accept/reject step* We compute the so-called Hastings ratio r , defined by:

$$r = \min \left(1, \frac{p(\hat{\Theta}|\mathcal{O})q(\Theta_n|\hat{\Theta})}{p(\Theta_n|\mathcal{O})q(\hat{\Theta}|\Theta_n)} \right) \quad (2.24)$$

Noteworthy, the Hastings ratio r is independent of the quantity $p(\mathcal{O})$. The new set of parameters $\hat{\Theta}$ is accepted or rejected with probability r :

$$\Theta_{n+1} = \begin{cases} \hat{\Theta} & \text{if } u < r \\ \Theta_n & \text{otherwise} \end{cases} \quad (2.25)$$

where u is a random variable sampled from the uniform distribution $\mathcal{U}(0, 1)$.

2.2.4 Numerical experiments

Experiments on synthesized random sets

To illustrate our methodology, we consider two examples of microstructures generated with morphological models. Our objective is to recover the parameterization of these models from statistical measurements conducted on realizations of the models. To that end, for each example, we generate a set of $N = 10$ random microstructures in a domain of size 30 by 30 in \mathbb{R}^2 .

- The first model corresponds to a Boolean model of disks with constant radii $R = 0.5$ and with intensity $\theta = 0.45$.
- The second model corresponds to a Cox-Boolean model of disks corresponding to a two scales microstructure, with the first scale consisting in exclusion zones that remain empty of any inclusions, modeled by a Boolean model of disk with constant radii $R_e = 1$ and intensity $\theta_e = 0.1$. The second scale simulates inclusions located in the complementary of the exclusion zones. The inclusions are described by a Boolean model of disks with intensity $\theta = 0.45$ and radii sampled according to a normal distribution with mean $R = 0.5$ and standard deviation 0.1.

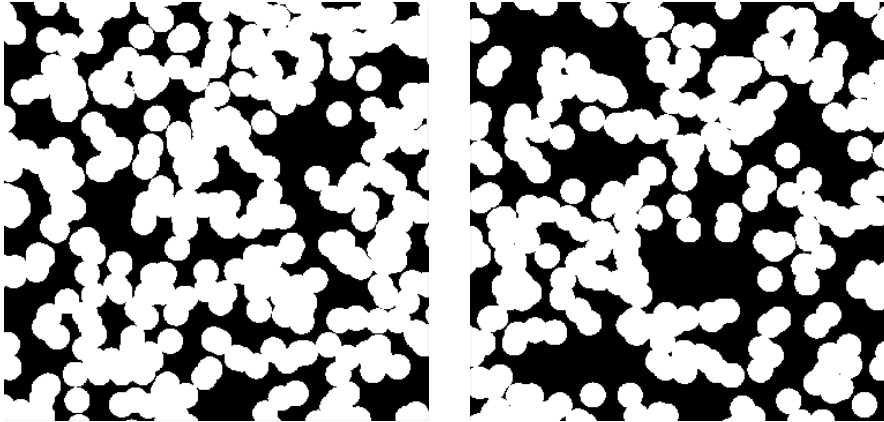


Figure 2.5: Sample of the microstructure generated with the Boolean model of disks (left) and with the Cox-Boolean model (right).

Realizations of both morphological models are displayed in Fig. 2.5. To obtain a set of measurements $m_{\mathcal{O}}$ for each morphological model, we averaged the covariance, the granulometry and the granulometry of the complementary as computed on 10 model realizations.

The upper and lower bounds for the parameters used to define the prior distribution are indicated in table 2.2 for the Boolean model and in table 2.3 for the Cox-Boolean model. We consider the same diagonal covariance matrix Λ in the likelihood function (2.15) for both morphological models. To put more emphasis on the correlations at the smallest scales, we employ the following expression for the diagonal coefficients of Λ :

$$\Lambda_{n,n} = \lambda \left(1 + \frac{1}{n} \right)^{-1}, \quad (2.26)$$

where $\lambda = 0.1$. Next, we initialize the Metropolis-Hastings algorithm by sampling a first set of parameters $\Theta_1 := (\theta_1, R_1)$ from the prior distribution. At each step of the algorithm, the proposal distribution for each parameter is the truncated normal distribution:

$$q(\theta|\theta_n) = \mathcal{N}_{tr}(\theta_n, \sigma_\theta, \theta_{min}, \theta_{max}), \quad (2.27)$$

where θ_{min} (resp. θ_{max}) is the minimal (resp. maximal) possible value of the parameter as established for defining the prior distribution, and the standard deviation σ is set to:

$$\sigma_\theta = \frac{\theta_{max} - \theta_{min}}{\Delta}. \quad (2.28)$$

	$\theta [L^{-1}]$	$R [L]$
Target	0.45	0.5
$\hat{\Theta}$	0.44 ± 0.05	0.52 ± 0.025
Min. Val.	0.2	0.15
Max. val.	0.9	1.05

Table 2.2: Optimal parameters found by the Metropolis-Hastings algorithm for the Boolean model of disks.

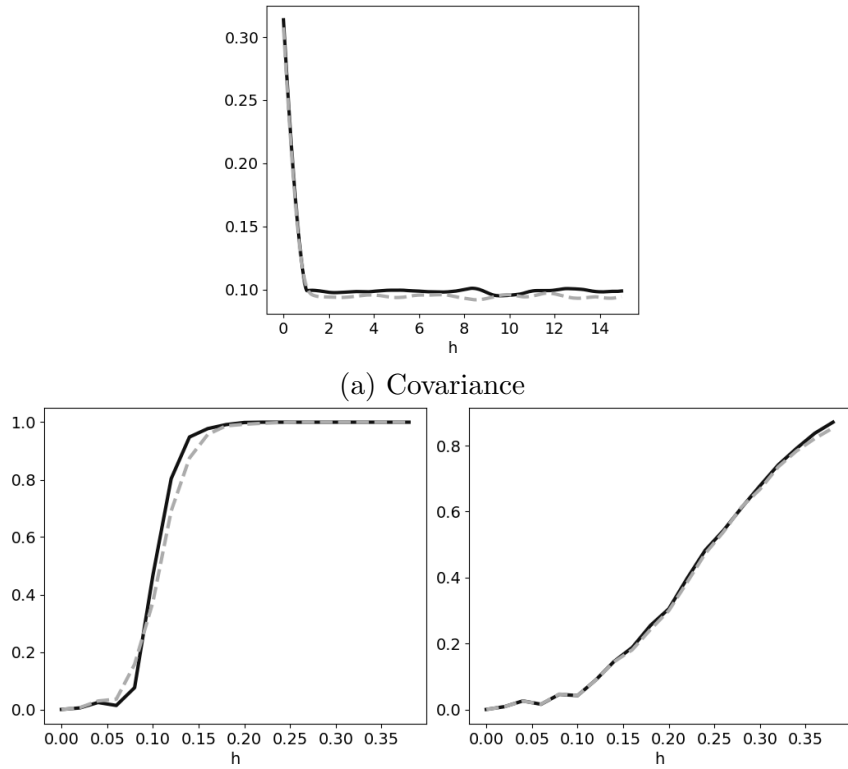
We fix $\Delta = 20$ to get an acceptance rate of 0.3 in the algorithm.

We stop the algorithm after 500 iterations, and we discard the first 100 parameters sampled by the algorithm, as they remain highly dependent on the initial conditions. Finally, we estimate the set of optimal parameters for the microstructure by considering the maximal a posteriori (MAP) value found for the sampled parameters:

$$\hat{\Theta} := \arg \max_{n=100, \dots, 500} p(\Theta_n | \mathcal{O}). \quad (2.29)$$

Results and discussion The optimal set of parameters $\hat{\Theta}$ found by the Metropolis-Hastings algorithm are displayed in Tab. 2.2 for the Boolean model of disks, along with the standard deviation of the sampled parameters, and in Tab. 2.3 for the Cox-Boolean model. The standard deviation provides valuable information about the sensitivity of the parameters: if a parameter has experienced only minor variations throughout the iterations of the algorithm, it implies that when this parameter deviates from its optimal value, there is a substantial deviation from the targeted measurements. In other words, even small changes in the parameter can have a significant impact on the agreement between the predicted measurements and the desired outcome. Overall, we can note that there is a good agreement between the parameters identified by the algorithm and the ones corresponding to the experimental microstructure. A comparison between the measurements as conducted on the target microstructures simulated with both morphological models and as obtained with the optimal set of parameters $\hat{\Theta}$ is displayed in Fig. 2.6 and 2.7. Again, we note a fairly good agreement between the measurements.

Fig. 2.8 displays a scatterplot of the parameters sampled by the Metropolis-Hastings algorithm for both morphological models. Interestingly, we note

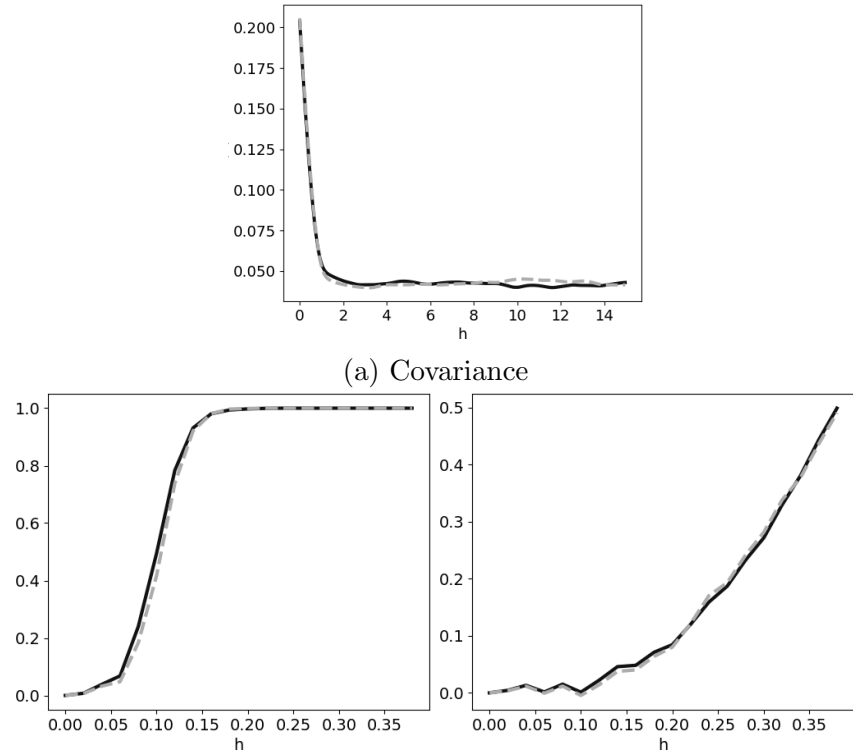


(b) Granulometry measurements of the microstructure (left) and of the complementary (right)

Figure 2.6: Comparison between the experimental measurements and the measurements obtained with simulations conducted with the MAP parameters identified by the MCMC algorithm for the Boolean model of disks .

	$\theta_e [L^{-1}]$	$R_e [L]$	$\theta [L^{-1}]$	R
Target	0.1	1.	0.45	0.5
$\hat{\Theta}$	0.13	0.85	0.45	0.5
Std. Dev.	0.03	0.25	0.05	0.04
Min. Val.	0.05	0.5	0.2	0.15
Max. val.	0.2	2.	0.9	1.05

Table 2.3: Optimal parameters found by the Metropolis-Hastings algorithm for the Cox-Boolean model of disks.



(b) Granulometry measurements of the microstructure (left) and of the complementary (right)

Figure 2.7: Comparison between the experimental measurements and the measurements obtained with simulations conducted with the MAP parameters identified by the MCMC algorithm for the Cox-Boolean model of disks.

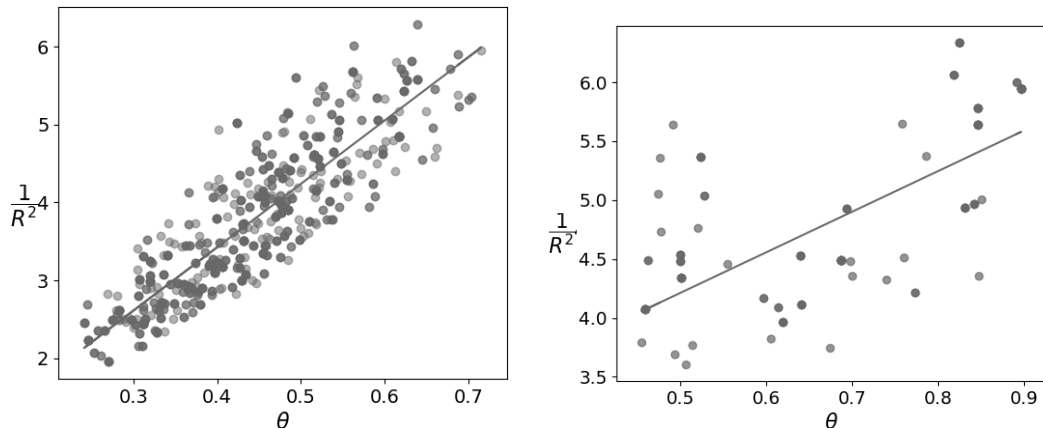


Figure 2.8: Scatterplot of the parameters $1/R^2$ and θ sampled by the Metropolis-Hastings algorithm for the Boolean model of disks (left) and for the Cox-Boolean model (right). The color intensity of each point corresponds to the frequency of the corresponding parameters within the samples.

that the parameters θ and R sampled by the algorithm are strongly correlated in the case of the Boolean model of disks. We performed a linear regression between the parameters θ and $1/R^2$, to find a coefficient of determination equal to 0.81. For a Boolean model of disks, the volume fraction v is known to be given by

$$v = 1 - \exp(\pi R^2 \theta). \quad (2.30)$$

This leads to the linear relationship

$$\frac{1}{R^2} = -\frac{\pi}{\log(1-v)}\theta. \quad (2.31)$$

The covariance measurements are highly sensitive to the volume fraction. Hence, by construction, the Metropolis-Hastings will usually select a set of parameters that allows to obtain a volume fraction similar to the one measured on the experimental samples. As evidenced in Fig. 2.8, the parameters are indeed distributed around a straight line. For the Cox-Boolean model, we note that the parameters θ and R sampled by the algorithm remain correlated, but the correlation is less obvious than for the Boolean model. A linear regression performed between the parameters θ and $1/R^2$ yields a coefficient of determination equal to 0.51. Due to the presence of exclusion zones in the

microstructure, Eq. (2.31) is not valid anymore, which explains this reduced correlation.

Experiments on experimental materials

In this section, we demonstrate the application of our proposed optimization approach to investigate an experimental microstructure. The microstructure under examination consists of pigments embedded in a matrix, forming a colloid film. These pigments possess an elongated ellipsoidal shape similar to that of a needle. To capture the microstructure for analysis, a dataset of experimental images was acquired using transmission electron microscopy (TEM) imaging. Figure 2.10 provides an illustrative example of one such TEM image. The analysis of the experimental TEM images reveals a noticeable tendency of the pigments to aggregate within the microstructure, resulting in the formation of clusters. These clusters exhibit a characteristic size that significantly exceeds the individual pigment size.

To describe the microstructure, we use a two-scale model as follows:

- The first scale of the simulation describes the pigments aggregates through a Boolean model of inclusion spheres characterized by two parameters, namely the intensity θ_i of the Poisson point \mathcal{P} process used to construct the Boolean model and the radii R_i of the spheres.
- The second scale of the model simulates the pigments within the aggregates using a Boolean model of ellipsoids whose largest semi-axis follows a normal law with mean L and standard deviation σ_L , and whose smallest semi-axes follow a normal law with mean l and standard deviation σ_l . A hardcore distance h is introduced in the underlying point process. Ellipsoids are implanted at locations sampled from a Poisson point process with intensity θ restricted to the set constituted by the spheres constitutive of the first scale of the model. Ellipsoids belonging to the same inclusion sphere share the same orientation, sampled uniformly from Euler's angles.

θ_i (μm^{-3})	R_i (μm)	θ (μm^{-3})	L (μm)	l (μm)	h (μm)
0.56	0.54	45.	0.56 ± 0.08	0.07 ± 0.01	0.2

Table 2.4: Optimal parameters for the "needles" microstructure.

2.2. PARAMETERS ESTIMATION IN MORPHOLOGICAL MODELS 73

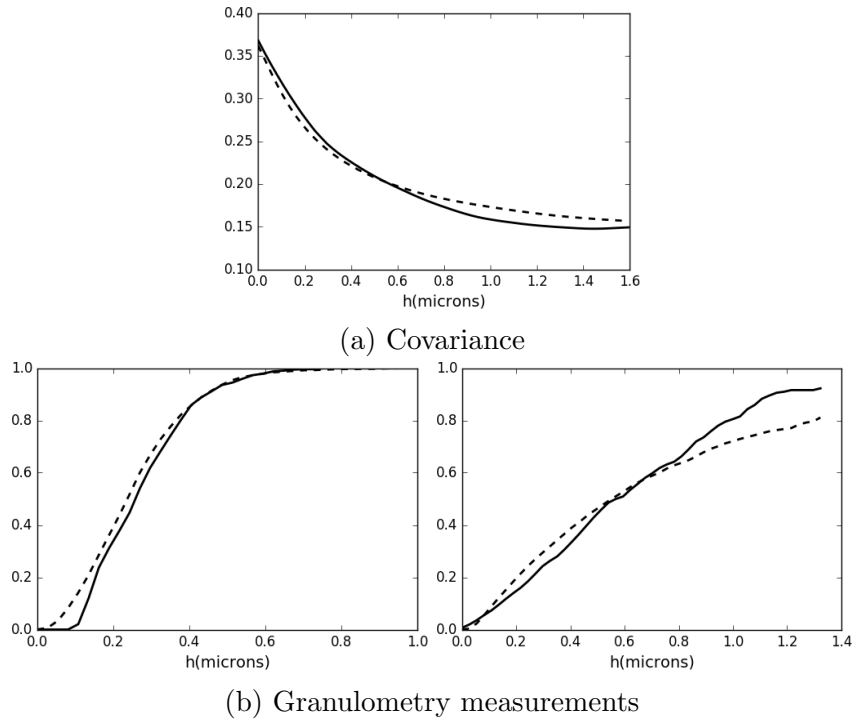


Figure 2.9: Comparison between the covariance and the granulometries as obtained on the experimental TEM images (dashed lines) and on the simulated TEM images for the "needles" microstructure [16].

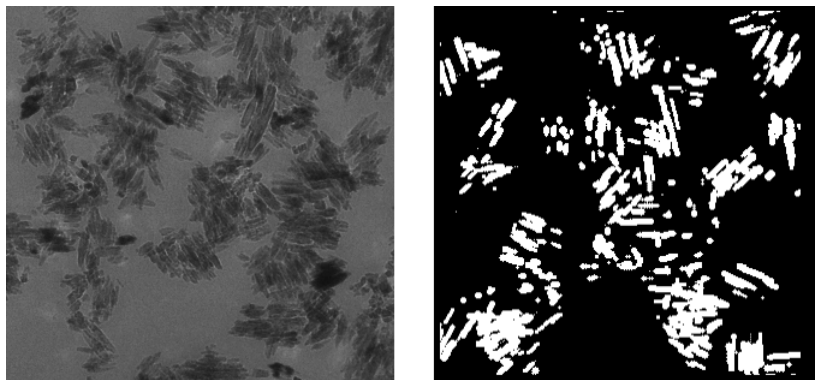


Figure 2.10: Needles microstructure: experimental TEM image (left) and binary image simulated with the morphological model using the optimal set of parameters identified by the Bayesian approach [16].

The description of the microstructure model requires eight parameters. These parameters include the intensity θ_i of the Poisson point process for the aggregates, their radius R_i , the lengths of the semi-axes L and l of the pigments, along with their corresponding standard variations σ_L and σ_l , the intensity θ of the point process used for the pigments and the hardcore distance h .

To determine the model parameters, we employ the Bayesian approach explained in the preceding section. We initiate the Metropolis-Hastings algorithm by setting λ to 1 during the simulation, and we terminate the algorithm after 200 iterations. Similar to before, we estimate the optimal parameter set for the microstructure by selecting the sample that exhibits the highest posterior probability among all the sampled parameters. Throughout the MCMC run, we generate TEM images of the microstructure by first creating a 3D sample of the model, then extracting a thick slice from the 3D volume that matches the thickness of the experimental slices used for obtaining the TEM images, and finally projecting the thick slice onto a single plane. An illustrative example of the microstructure generated using this approach is presented in Figure 2.10. Covariance and granulometry measurements are subsequently performed on both the experimental and simulated TEM images.

The optimal set of parameters $\hat{\Theta}$ determined by the Metropolis-Hastings algorithm for the morphological model is shown in Table 2.4. A comparison is presented in Figure 2.9 between the measurements conducted on the experimental microstructure and those obtained using the optimal set of parameters. We observe that the optimal parameter set enables us to achieve a good agreement between the experimental measurements and the measurements performed on simulations of the morphological models.

2.2.5 Conclusion

In this section, we presented a Bayesian approach for determining the parameters of morphological models of microstructure using measurements obtained from experimental microstructure images. Through various examples, we demonstrated that this approach effectively identifies the optimal parameters for different morphological models and detects potential correlations among the model parameters. Our proposed methodology offers several advantages compared to other parameter determination approaches. Specifically, it eliminates the need for computing the gradient of the model with

respect to the parameters and provides a sequence of parameter samples, enabling the quantification of the parameters sensitivity and the identification of potential correlations between them.

2.3 Eikonal based tessellations

We present in this section a research work that establishes a link between the Johnson-Mehl and Voronoï tessellation models and the Eikonal equation on a domain. A direct incentive for this study was the development of efficient algorithms for generating the tessellations used to simulate the interstices of the coldspray microstructure considered in section 2.1. We base the writing of this section on the article [14] published in 2019 in *Image Analysis & Stereology* and related to this research study. The analogy established between the Voronoï tessellation and the Eikonal equation has two direct applications: the generation of images of the tessellation in an efficient manner, and the generation of tessellations with rough boundaries.

2.3.1 Eikonal equation

The Eikonal equation describes the propagation of a wave on an open domain Ω through the non-linear partial differential equation:

$$\forall x \in \Omega, \quad \nabla t(x) = \frac{1}{u(x)}. \quad (2.32)$$

In Eq. (2.32), ∇ denotes the gradient operator, and $t(x)$ and $u(x)$ represent the first arrival time of the wave at point x and the velocity of the wave at location x , respectively.

In order to compute the image of a Johnson-Mehl tessellation on a domain Ω , let us consider the specific version of the Eikonal equation. Given a Poisson point process \mathcal{P} with realizations $(x_i)_{i=1,\dots,N}$ and corresponding germination times $(\tau_i)_{i=1,\dots,N}$, we consider the problem:

$$\begin{cases} \nabla t(x) = \frac{1}{u(x)} \\ t(x_i) = \tau_i, \forall i = 1, \dots, N. \end{cases} \quad (2.33)$$

If the velocity $u(x)$ is constant, then we can use the following proposition (see [48]):

Proposition 2.3.1. *On the domain Ω , the solution t of problem (2.33) satisfies, for all $x \in \Omega$,*

$$t(x) = \inf_{i=1,\dots,N} (t_i + \|x - x_i\|^2). \quad (2.34)$$

Proposition 2.3.1 states that solving the Eikonal equation is an efficient way to compute the Johnson-Mehl distance on a grid of points, as it precisely matches the distance used for constructing the Johnson-Mehl tessellation. Efficient algorithms are available for this task, including the fast marching algorithm described in the next section [48, 11].

2.3.2 Fast marching algorithm

The fast marching (FM) algorithm compute the arrival times in the domain iteratively by following the propagation of the waves coming from the germs. Here, we present a slightly adapted version of the fast marching algorithm that keeps track of the labels of the initial germs during the propagation, in order to facilitate the generation of the Johnson-Mehl tessellation. We restrict ourselves to the 2D framework to keep notations simple. We initialize the algorithm as follows:

1. We initialize the map of *arrival times* by setting the arrival at each voxel x_i equal to $t_i = \infty$, except if the considered voxel contains a germ from \mathcal{P} . In this case, the arrival time at x_i is set to be the germination time τ_j .
2. We initialize a map of *labels* that keeps tracks of the wave that has arrived at each location first. We affect the label j to the voxels x_i containing one of the germs $(g_j)_{1 \leq j \leq N}$ are associated the label j . We affect the label 0 to the other voxels.
3. Finally, we group all voxels containing one of the germ in a set referred to as the *narrow band*.

At each iteration, we extract the voxel (X, Y) of the narrow band with smallest arrival time and we affect it to the *frozen set*. Next, we compute the arrival times of the wave at all neighboring voxels and we add these voxels to the

narrow band. At each neighbor location (x, y) of (X, Y) , we compute the arrival time by solving Eikonal equation

$$\|\nabla T\|(x, y)u(x, y) = 1. \quad (2.35)$$

The main difficulty at this point is to propose a discretization for the gradient term. Following the work [48], we discretize Eikonal equation in the following manner

$$\begin{aligned} & (t_{x,y} - \min(t_{x,y+1}, t_{x,y-1}))^2 + \\ & (t_{x,y} - \min(t_{x+1,y}, t_{x-1,y}))^2 = \frac{1}{u(x, y)^2} \end{aligned} \quad (2.36)$$

In Eq. (2.36), the use of the min operator ensures that the information propagates from the already computed neighbors, which is essential for the stability of the fast marching method. Equation (2.36) is quadratic in $t_{x,y}$ and admits two solutions. To respect the causality principle, we select the largest solution of (2.36). This choice guarantees that the wave propagates forward in time and maintains the consistency of the numerical scheme.

Once the arrival time $t(x, y)$ has been computed, we can encounter two distinct situations:

- When the neighbor point (x, y) is in the narrow band, it means that it has already been affected an arrival time $t^{old}(x, y)$. If $t(x, y) < t_{old}(x, y)$, then we affect the arrival time $t(x, y)$ to (x, y) as well as the label of point (X, Y) . On the contrary, if $t(x, y) > t_{old}(x, y)$, the label and the arrival time at (x, y) remain unchanged.
- When the neighbor point (x, y) is not in the narrow band, we affect to it the arrival time $t(x, y)$ as well as the label of (X, Y) , and we add it to the narrow band.

At each iteration of the algorithm, it is necessary to extract the element of the narrow band with the smallest arrival time. To sort the elements of the narrow band in an efficient manner, we use a binary heap to store them. We refer the reader interested by more details on the fast marching algorithm implementation to the original articles [28, 48, 49].

2.3.3 Applications

We describe in this section two potential applications of the proposed approach for generating a tessellation: the first application describes a computationally efficient method for generating an image of a Voronoï or Johnson-Mehl tessellation from a set of germs. The second application is related to the generation of tessellation with rough boundaries that it is made possible by the use of Eikonal equation.

Generation of images from vectorial simulations

For materials engineering applications, it is often necessary to simulate images of a generated Voronoï or Johnson-Mehl tessellation. In practice, the tessellation is entirely characterized by the location of its germs and by the corresponding implantation times in the case of the Johnson-Mehl tessellation. The image generation is achieved by discretizing the domain Ω and by evaluating the implicit functions associated with the tessellation's cells at each voxel location. However, this approach can be computationally expensive, particularly when high resolution is required. If we denote the number of voxels used to discretize Ω as P , the average number of Poisson points in \mathcal{P} is proportional to P . As a result, the image generation algorithm's complexity is $O(P^2)$, which can represent a significant amount of computation when using this method for a vectorial simulation. By contrast, using the approach based on the Eikonal equation yields a complexity in $O(N \log N)$, which is particularly appealing for large values of N .

Tessellation with rough boundaries

We have considered so far a constant velocity field u in the Eikonal equation (2.33) for constructing the Johnson-Mehl tessellation. However, when using the Eikonal equation to build the mosaic, it is possible to use any velocity fields on the domain Ω , as long as $u(x) > 0$ for all $x \in \Omega$. This observation opens the way to the development of tessellation models that cannot be directly obtained with classical approaches including the Voronoï and the Johnson-Mehl tessellations described previously. A potential application is for instance the generation of tessellations of space with rough boundaries between adjacent cells.

Let \mathcal{P} be the realization of a marked point process with intensity θ on an open domain Ω , for which the marks are drawn according to the uniform

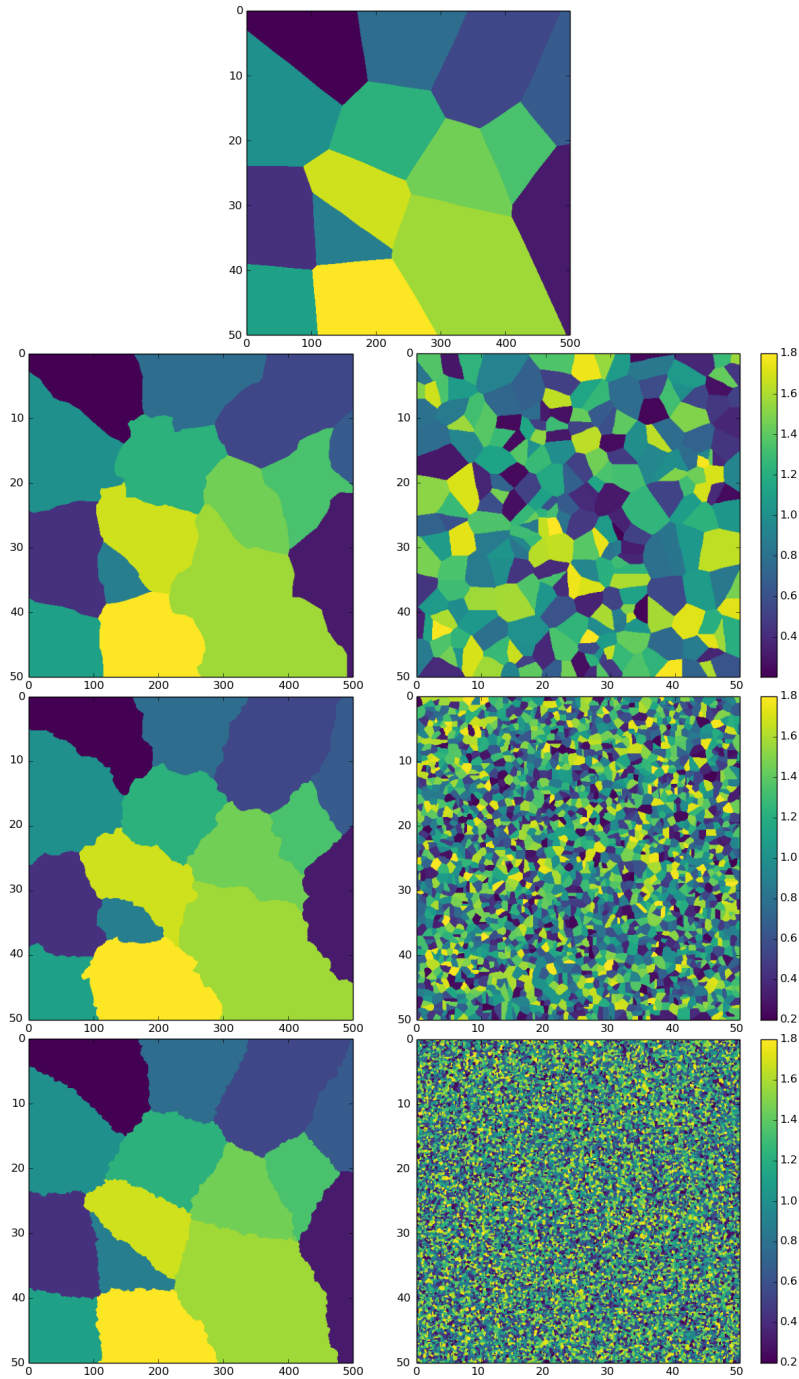


Figure 2.11: Rough Voronoï tessellations (left) and corresponding local velocity field (right). The tessellations were generated with the same set of germs \mathcal{P} on a 50×50 domain, discretized on a 500×500 regular grid. The local velocity fields are realizations of Voronoï tessellations with respective intensities $\theta = 0$, $\theta = 0.1$, $\theta = 1$ and $\theta = 10$.

distribution $\mathcal{U}([0, L])$ on an interval $[0, L] \subset \mathbb{R}_+$. The points in \mathcal{P} as well as their respective marks allow to compute a Johnson-Mehl tessellation on the domain Ω by solving problem (2.33). We construct a random velocity field u on domain Ω by

1. computing a Voronoï tessellation of Ω based upon a Poisson point process \mathcal{P}_v with intensity θ_v , and
2. setting a random velocity drawn according to some distribution \mathcal{D} in each cell of the Voronoï tessellation.

By solving the problem

$$\begin{cases} \nabla t(x) = \frac{1}{u(x)} \\ t(x_i) = \tau_i, \forall i = 1, \dots, N \end{cases} \quad (2.37)$$

we obtain a tessellation of the domain Ω resembling the Johnson-Mehl tessellation generated by solving (2.33), but with rough boundaries between adjacent cells. It is worth noting that the roughness observed at the boundaries is closely linked to the characteristic length of the fluctuations in the velocity field. This characteristic length is dependent on the intensity of the Voronoï tessellation, denoted by θ_v , which is used to compute the velocity field. A larger value of θ_v results in a greater number of smaller Voronoï cells, leading to velocity variations over shorter distances. As a result, the generated Johnson-Mehl tessellation displays boundaries with a high concentration of roughness patterns with relatively small amplitudes. In contrast, Johnson-Mehl tessellations generated from velocity fields constructed with a smaller value of θ_v exhibit boundaries with a lower density of roughness patterns with larger amplitudes. In the original article [14], we developed a multi-scale tortuosity descriptor, which is able to characterize the tortuosity of the boundary between two adjacent cells by iteratively computing the tortuosity of smoothed versions of the boundary. This descriptor allowed us to establish a direct correlation between the value of θ_v and the tortuosity of the boundaries at distinct scales. We refer the reader interested by additional details to the original article [14].

To illustrate our algorithm, we present in figure 2.11 simulations of Voronoï tessellations with rough boundaries computed with different values of velocity parameter θ_v . In this figure, we generated four distinct Voronoï tessellations

on a domain with size 50×50 discretized on a 500×500 regular grid. To generate the tessellation, we started from the same realization of a Poisson point process \mathcal{P} with intensity $\theta = 5 \times 10^{-2}$. We generated a random velocity field for each one of the tessellations by first constructing a Voronoï tessellation of the domain, and then selecting a random velocity drawn from the uniform distribution \mathcal{U} on the interval $[0.2, 1.8]$ for each cell of the tessellation. The characteristic length λ_v of the velocity variation can be related to the intensity θ_v of the point process used to construct the germs of the tessellation through the relationship []

$$\lambda_v \simeq \sqrt{\frac{1}{\theta_v}}.$$

We note that when λ_v is small, it leads to the obtaining of small roughness patterns at the cell boundaries. Conversely, large values of λ_v lead to larger sizes of roughness pattern. The proposed method therefore allows to control, at least qualitatively, the amplitude and the size of the roughness patterns observed at the boundaries.

2.3.4 Conclusion

In this section, we established a direct connection between Johnson-Mehl and Voronoï tessellations and the Eikonal equation, showing that the construction of such tessellations can be reformulated as a wave propagation problem. This interpretation provides both theoretical insight and practical advantages. In particular, solving the Eikonal equation with appropriate initial conditions enables an efficient computation of tessellations through the fast marching algorithm, significantly reducing computational complexity compared to classical voxel-wise evaluation methods.

Beyond computational efficiency, the Eikonal framework also offers increased modeling flexibility. By introducing spatially varying velocity fields, we demonstrated that it is possible to generate tessellations with controlled boundary roughness, extending classical Voronoï and Johnson-Mehl models. The characteristic length of the velocity fluctuations directly governs the amplitude and scale of boundary irregularities, providing a simple and intuitive way to tune geometric complexity.

Overall, the Eikonal-based formulation constitutes a powerful and versatile approach for the simulation of tessellated microstructures, with direct applications to morphological modeling and materials science.

Bibliography

- [1] H. Altendorf and D. Jeulin. Random-walk-based stochastic modeling of three-dimensional fiber systems. *Physical Review E*, 83(4):041804, 2011.
- [2] O. Amsellem, K. Madi, F. Borit, D. Jeulin, V. Guipont, M. Jeandin, E. Boller, and F. Pauchet. Two-dimensional (2d) and three-dimensional (3d) analyses of plasma-sprayed alumina microstructures for finite-element simulation of young's modulus. *Journal of Materials Science*, 43(12):4091–4098, 2008.
- [3] Christophe Andrieu, Nando De Freitas, Arnaud Doucet, and Michael I Jordan. An introduction to mcmc for machine learning. *Machine learning*, 50:5–43, 2003.
- [4] M. Avrami. Kinetics of phase change. I. general theory. *The Journal of Chemical Physics*, 7(12):1103–1112, 1939.
- [5] F. Baccelli and B. Blaszczyszyn. *Stochastic Geometry and Wireless Networks: Volume 1: THEORY*, volume 1. Now Publishers Inc, 2009.
- [6] S. Beauvais, V. Guipont, M. Jeandin, D. Jeulin, A. Robisson, and R. Saenger. Study of the porosity in plasma-sprayed alumina through an innovative three-dimensional simulation of the coating buildup. *Metallurgical and Materials Transactions A*, 39(11):2711–2724, 2008.
- [7] Vincent Bortolussi, Bruno Figliuzzi, François Willot, Matthieu Faessel, and Michel Jeandin. Morphological modeling of cold spray coatings. *Image Analysis & Stereology*, 37(2):145–158, 2018.
- [8] Vincent Bortolussi, Bruno Figliuzzi, François Willot, Matthieu Faessel, and Michel Jeandin. Electrical conductivity of metal–polymer cold spray

- composite coatings onto carbon fiber-reinforced polymer. *Journal of Thermal Spray Technology*, 29:642–656, 2020.
- [9] V. Capasso. *Mathematical Modelling for Polymer Processing: Polymerization, Crystallization, Manufacturing*, volume 2. Springer, 2003.
 - [10] S. N. Chiu, D. Stoyan, W. S. Kendall, and J. Mecke. *Stochastic geometry and its applications*. John Wiley & Sons, 2013.
 - [11] Eva Dejnozková and Petr Dokládal. A parallel algorithm for solving the eikonal equation. In *2003 IEEE International Conference on Acoustics, Speech, and Signal Processing, 2003. Proceedings.(ICASSP'03)*., volume 3, pages III–325. IEEE, 2003.
 - [12] F. Delloro, M. Faessel, H. Proudhon, D. Jeulin, M. Jeandin, E. Meillot, and L. Bianchi. A morphological approach to the modeling of the cold spray process. In *ITSC 2014*, pages 221–226. DVS, 2014.
 - [13] M. Faessel. Vtksim software.
 - [14] Bruno Figliuzzi. Eikonal-based models of random tessellations. *Image Analysis & Stereology*, 38(1):15–23, 2019.
 - [15] Bruno Figliuzzi, WHR Chan, CR Buie, and JL Moran. Nonlinear electrophoresis in the presence of dielectric decrement. *Physical Review E*, 94(2):023115, 2016.
 - [16] Bruno Figliuzzi, Antoine Montaux-Lambert, François Willot, Grégoire Naudin, Pierre Dupuis, Bernard Querleux, and Etienne Huguet. A bayesian approach to morphological models characterization. *Image Analysis & Stereology*, 40(3):171–180, 2021.
 - [17] E. N. Gilbert. Random subdivisions of space into crystals. *The Annals of mathematical statistics*, pages 958–972, 1962.
 - [18] P. Hall. *Introduction to the theory of coverage processes*, volume 188. Wiley New York, 1988.
 - [19] H Hermann. Stochastic models of heterogeneous materials. In *Materials science forum*. Trans Tech Publications, 1991.

- [20] A. Jean, D. Jeulin, S. Forest, S. Cantournet, and F. N'Guyen. A multi-scale microstructure model of carbon black distribution in rubber. *Journal of microscopy*, 241(3):243–260, 2011.
- [21] D. Jeulin. *Models of random structures*. Lecture notes.
- [22] D. Jeulin. Morphology and effective properties of multi-scale random sets: A review. *Comptes Rendus Mécanique*, 340(4):219–229, 2012.
- [23] D. Jeulin, P. Monnaie, and F. Péronnet. Gypsum morphological analysis and modeling. *Cement and Concrete Composites*, 23(2):299–311, 2001.
- [24] D. Jeulin and M. Moreaud. Percolation of multi-scale fiber aggregates. In *S4G, 6th International Conference Stereology, Spatial Statistics and Stochastic Geometry. Prague*, pages 26–29, 2006.
- [25] Dominique Jeulin. *Morphological models of random structures*. Springer, 2021.
- [26] W. A. Johnson and R. F. Mehl. Reaction kinetics in processes of nucleation and growth. *Trans. Aime*, 135(8):396–415, 1939.
- [27] André Liebscher and Claudia Redenbach. Statistical analysis of the local strut thickness of open cell foams. *Image Analysis & Stereology*, 32(1):1–12, 2013.
- [28] Ravi Malladi, James A Sethian, and Baba C Vemuri. Shape modeling with front propagation: A level set approach. *IEEE transactions on pattern analysis and machine intelligence*, 17(2):158–175, 1995.
- [29] G. Matheron. *Random sets and integral geometry*, volume 1. Wiley New York, 1975.
- [30] J. Mecke. Palm methods for stationary random mosaics. *Combinatorial principles in stochastic geometry*, pages 124–132, 1980.
- [31] J. Mecke. Inequalities for the anisotropic poisson polytope. *Advances in applied probability*, pages 56–62, 1995.
- [32] R. E. Miles. The random division of space. *Advances in applied probability*, pages 243–266, 1972.

- [33] R. E. Miles. Estimating aggregate and overall characteristics from thick sections by transmission microscopy. *Journal of Microscopy*, 107(3):227–233, 1976.
- [34] I. S. Molchanov. Statistics of the boolean model: from the estimation of means to the estimation of distributions. *Advances in applied probability*, pages 63–86, 1995.
- [35] J. Møller. Random tessellations in \mathbb{R}^d . *Advances in Applied Probability*, pages 37–73, 1989.
- [36] J. Møller. Random johnson-mehl tessellations. *Advances in applied probability*, pages 814–844, 1992.
- [37] Jesper Møller. *Lectures on random Voronoi tessellations*. Springer, 1994.
- [38] Maxime Moreaud, Dominique Jeulin, Vincent Morard, and Renaud Revel. Tem image analysis and modelling: application to boehmite nanoparticles. *Journal of microscopy*, 245(2):186–199, 2012.
- [39] Joachim Ohser and Katja Schladitz. *3D images of materials structures: processing and analysis*. John Wiley & Sons, 2009.
- [40] Ch. Peyrega, D. Jeulin, Ch. Delisée, and J. Malvestio. 3d morphological modelling of a random fibrous network. *Image Analysis & Stereology*, 28(3):129–141, 2011.
- [41] J.-L. Quenech, M. Coster, J.-L. Chermant, and D. Jeulin. Study of the liquid-phase sintering process by probabilistic models: Application to the coarsening of WC-Co cermets. *Journal of Microscopy*, 168(1):3–14, 1992.
- [42] Claudia Redenbach. Microstructure models for cellular materials. *Computational Materials Science*, 44(4):1397–1407, 2009.
- [43] Claudia Redenbach and Irene Vecchio. Statistical analysis and stochastic modelling of fibre composites. *Composites Science and Technology*, 71(2):107–112, 2011.
- [44] Christian P Robert, George Casella, and George Casella. *Monte Carlo statistical methods*, volume 2. Springer, 1999.

- [45] L. A. Santaló. Integral geometry and geometric probability. 1976.
- [46] R. Schneider and W. Weil. *Stochastic and integral geometry*. Springer, 2008.
- [47] J. Serra. *Image analysis and mathematical morphology*. Academic press, 1982.
- [48] James A Sethian. A fast marching level set method for monotonically advancing fronts. *Proceedings of the National Academy of Sciences*, 93(4):1591–1595, 1996.
- [49] James A Sethian. Fast marching methods. *SIAM review*, 41(2):199–235, 1999.
- [50] S. Torquato. *Random heterogeneous materials: microstructure and macroscopic properties*, volume 16. Springer, 2002.
- [51] Haisheng Wang, Dominique Jeulin, François Willot, Loïc Sorbier, and Maxime Moreaud. Modelling of the microstructure of mesoporous alumina constrained by morphological simulation of nitrogen porosimetry. *Colloids and Surfaces A: Physicochemical and Engineering Aspects*, 553:378–396, 2018.
- [52] Haisheng Wang, Andrea Pietrasanta, Dominique Jeulin, François Willot, Matthieu Faessel, Loïc Sorbier, and Maxime Moreaud. Modelling mesoporous alumina microstructure with 3d random models of platelets. *Journal of microscopy*, 260(3):287–301, 2015.
- [53] Haisheng Wang, François Willot, Maxime Moreaud, Mickaël Rivallan, Loïc Sorbier, and Dominique Jeulin. Numerical simulation of hindered diffusion in γ -alumina catalyst supports. *Oil & Gas Science and Technology–Revue d’IFP Energies nouvelles*, 72(2):8, 2017.
- [54] W. Weil and J. A. Wieacker. Densities for stationary random sets and point processes. *Advances in applied probability*, pages 324–346, 1984.